# On-chip multi-degree-of-freedom control of two-dimensional materials

https://doi.org/10.1038/s41586-024-07826-x

Received: 18 April 2024

Accepted: 12 July 2024

Published online: 21 August 2024



Haoning Tang¹, Yiting Wang¹, Xueqi Ni¹, Kenji Watanabe², Takashi Taniguchi², Pablo Jarillo-Herrero³, Shanhui Fan⁴, Eric Mazur¹⊠, Amir Yacoby⁵⊠ & Yuan Cao⁵,6,7⊠

Two-dimensional materials (2DM) and their heterostructures offer tunable electrical and optical properties, primarily modifiable through electrostatic gating and twisting. Although electrostatic gating is a well-established method for manipulating 2DM, achieving real-time control over interfacial properties remains challenging in exploring 2DM physics and advanced quantum device technology<sup>1-6</sup>. Current methods, often reliant on scanning microscopes, are limited in their scope of application, lacking the accessibility and scalability of electrostatic gating at the device level. Here we introduce an on-chip platform for 2DM with in situ adjustable interfacial properties, using a microelectromechanical system (MEMS). This platform comprises compact and cost-effective devices with the ability of precise voltage-controlled manipulation of 2DM, including approaching, twisting and pressurizing actions. We demonstrate this technology by creating synthetic topological singularities, such as merons, in the nonlinear optical susceptibility of twisted hexagonal boron nitride (h-BN)<sup>7-10</sup>. A key application of this technology is the development of integrated light sources with real-time and wide-range tunable polarization. Furthermore, we predict a quantum analogue that can generate entangled photon pairs with adjustable entanglement properties. Our work extends the abilities of existing technologies in manipulating low-dimensional quantum materials and paves the way for new hybrid two- and three-dimensional devices, with promising implications in condensed-matter physics, quantum optics and related fields.

Two-dimensional materials (2DM) emerge as a transformative class of materials with the potential to uncover new physics and device applications, because of their remarkable tunability by electrostatic gating and through van der Waals (vdW) stacking<sup>11</sup>. The introduction of twist in vdW stacks, together with intrinsic lattice mismatch, further offers control over their band structures and many-body correlations by moiré effects<sup>12-17</sup>.

For two decades, assembling vdW heterostructures has relied on dry and wet transfer  $^{18,19}$ . These methods are reliable, simple to implement and amenable to subsequent processing, such as etching and electrode evaporation. However, as the complexity of the stacks of 2DM continues to evolve, a limitation becomes increasingly evident. Each stack is inherently unique and non-reconfigurable  $^{20}$ . The associated non-reproducibility precludes convenient exploration of stacking parameters, such as twist angle, and many conclusions are reached only from a handful of samples.

Recently, an approach based on scanning microscopes has been proposed, allowing control of the twist angle and performing tunnelling spectroscopy simultaneously<sup>6</sup>. Although it represents a marked advancement, it requires a highly specialized and costly setup, and expertise that few laboratories possess<sup>1–5</sup>. These limitations indicate the need for a universal approach to manipulate the stacking in vdW

heterostructures at the device level. Here we design and implement an on-chip platform based on microelectromechanical systems (MEMS) for generic manipulation of 2DM with unprecedented flexibility and accuracy. This platform, named MEMS-based Generic Actuation platform for 2D materials (MEGA2D), not only addresses the need for insitu control over 2DM stacking but also provides a lot of opportunities in condensed-matter physics, optics and beyond. MEGA2D renders the stacking in a 2D heterostructure on par with electrostatic gating, in terms of convenience, scalability and accessibility to the broader research community. It is compatible and can be easily integrated into any existing transport and optical measurement systems.

#### Micromachine designed for twisting 2DM

Our objective is to tune the twist angle,  $\theta$ , and the separation distance, h, between two 2DM (Fig. 1a). Two primary challenges arise when using MEMS for manipulating 2DM: (1) MEMS actuators exhibit limited travel<sup>21,22</sup>, necessitating that the layers of 2DM be in close proximity (a few micrometres) at rest. Thermal expansion and magnetostriction, when working under conditions involving low temperatures and/or high magnetic fields, can further distort the MEMS. To maintain scalability, it is essential to preserve this initial gap without using an external

<sup>1</sup>School of Engineering and Applied Sciences, Harvard University, Cambridge, MA, USA. <sup>2</sup>National Institute for Materials Science, Tsukuba, Japan. <sup>3</sup>Department of Physics, Massachusetts Institute of Technology, Cambridge, MA, USA. <sup>4</sup>Department of Applied Physics and Ginzton Laboratory, Stanford University, Stanford, CA, USA. <sup>5</sup>Department of Physics, Faculty of Art and Sciences, Harvard University, Cambridge, MA, USA. <sup>6</sup>Society of Fellows, Harvard University, Cambridge, MA, USA. <sup>7</sup>Department of Electrical Engineering and Computer Science, University of California, Berkeley, Berkeley, CA, USA. <sup>∞</sup>e-mail: mazur@seas.harvard.edu; yacoby@g.harvard.edu; caoyuan@berkeley.edu

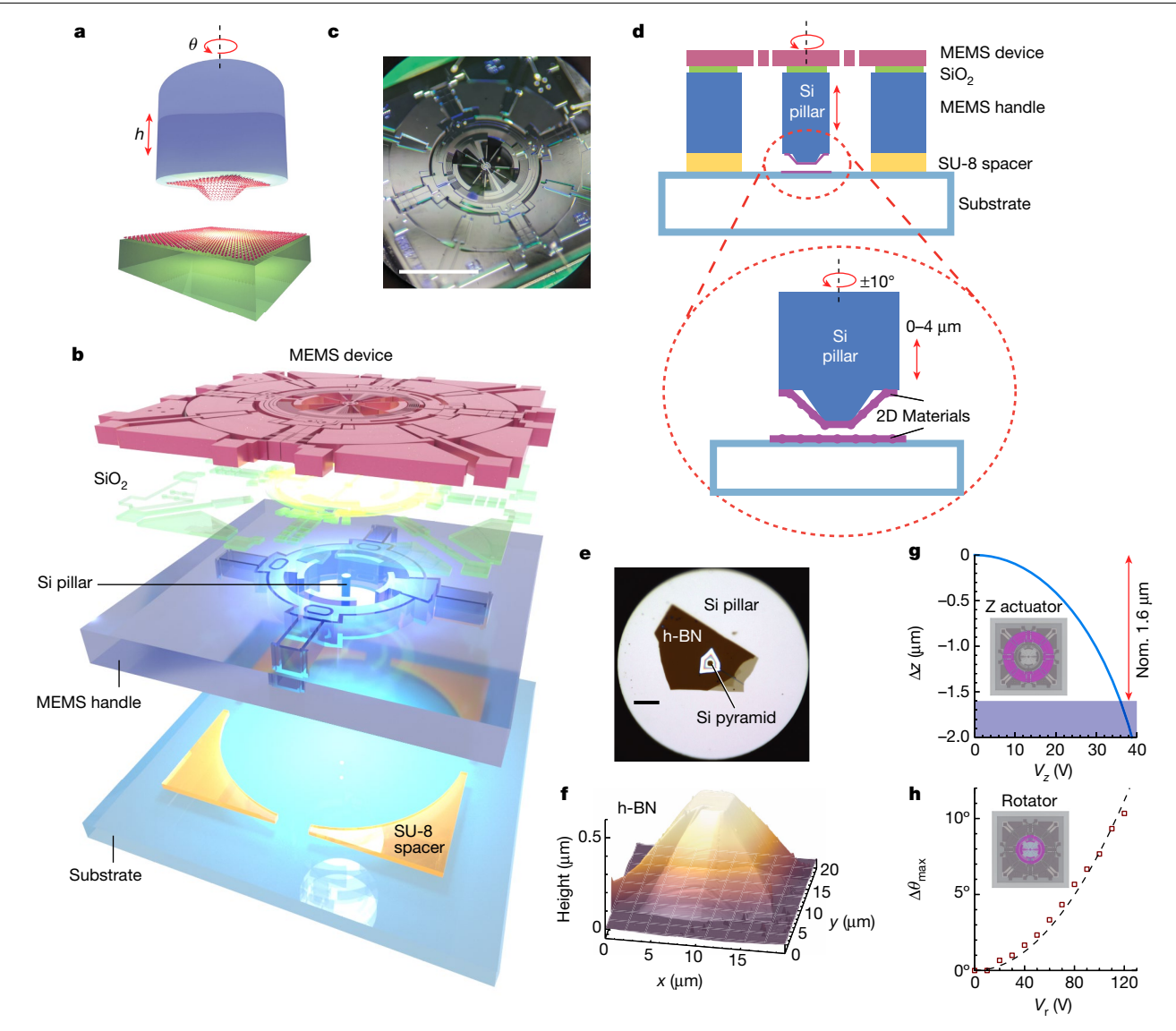


Fig. 1 | MEGA2D, an on-chip MEMS platform for twisting 2D materials. a, Illustration of the high-level idea of controlling the stacking in 2DM heterostructures using nanomechanical systems. We wish to control the twist angle  $\theta$  and distance h between two 2DM independently. **b**, Exploded schematic of the main components in a MEGA2D device. c, Photograph of a fully assembled MEGA2D device. Scale bar, 2 mm d, Cross-sectional schematic of an assembled MEGA2D device. At the bottom of the central silicon pillar (circled with red dashed lines and magnified in the bottom panel), the 2DM are integrated, one on the pyramid etched on the bottom of Si pillar and the other on the

substrate. e, Photograph of a piece of h-BN flake on the pyramid. Scale bar, 20 μm. f, AFM image of an h-BN flake on the pyramid with a height of about  $0.6 \, \mu m$ , exhibiting a flat surface at the top with a size of  $4 \times 4 \, \mu m^2$ . g, Calculated actuation curve of the MEMS vertical actuator. A control voltage of  $V_z \approx 38 \text{ V}$  is necessary to bring the pyramid into contact with the substrate. h, Measured and fitted actuation curves of the MEMS rotator. A rotation up to  $\pm 10^{\circ}$  can be achieved at a rotational control voltage of  $V_c = 120$  V. The fit curve is a quadratic curve with respect to  $V_r$ .

#### mechanical or piezo stage. (2) The mating interface between 2DM must be exceptionally flat and parallel to ensure consistent engagement.

Both challenges are resolved by design in MEGA2D (Fig. 1b). Each MEGA2D device is bonded from a top MEMS die and a bottom substrate using an SU-8 spacer. There are two main components in each MEMS die: a 60-µm silicon (Si) MEMS device layer and a 450-µm Si MEMS handle layer, separated by SiO<sub>2</sub>. Figure 1c,d shows an optical image and a cutaway schematic of a fully assembled MEGA2D device. At the core of MEGA2D is an Si pillar attached to the centre of the device layer, driven to translate vertically or rotate along its axis. At the bottom of the Si pillar, a pyramid is etched to provide a protruding platform, in which a flake of 2DM will be transferred<sup>6</sup> (Fig. 1d). A second flake of 2DM is placed on the substrate and aligned with the pyramid, which interacts with the on-pyramid 2DM as the MEMS is vertically translated or rotated. Figure 1e,f shows an optical image and an atomic force

microscopy (AFM) image of an h-BN flake on the pyramid, in which it forms a flat surface, the dimension of which is defined by the etched pyramid  $(4 \times 4 \mu m^2)$ . The complete device has a dimension of  $1 \times 1 \text{ cm}^2$ and can be mounted in any measurement apparatus without requiring any special equipment beyond a few electrical connections.

As the Si pillar and the handle layer are monolithically etched from the same wafer and have the same height (about 450 µm), thermal expansion and magnetostriction will have the same effect on both, and their effects on the distance between the 2DM cancel out. The flatness of the interface of the 2DM is also guaranteed, for which we estimate the tilt between the 2DM to be less than 0.01° and is further correctable (Methods). The free-standing distance between the 2DM is determined by the difference between the thickness of the SU-8 spacer and the height of the pyramid, which equals around 1.6 μm in our experiment and is highly reproducible.

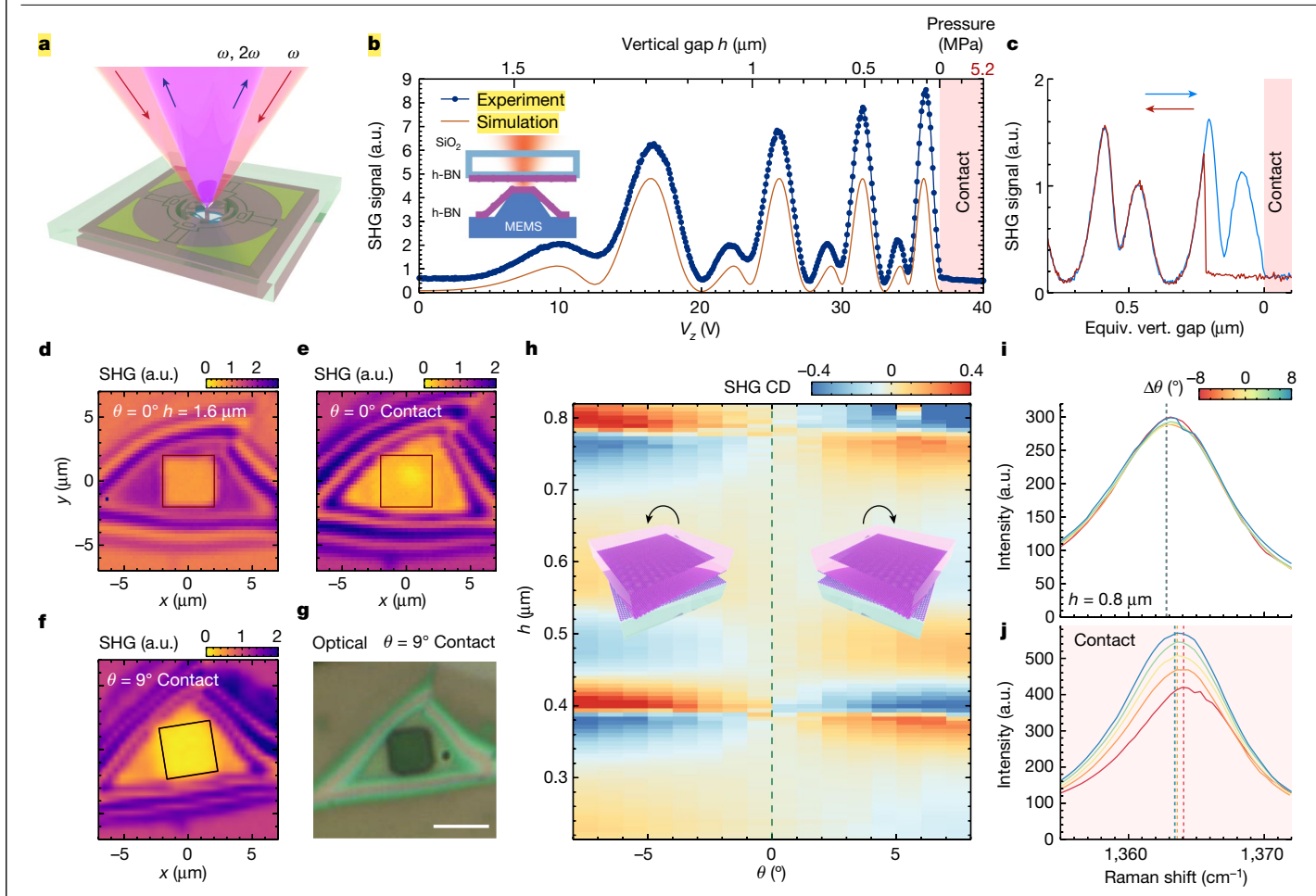


**Fig. 2** | **Nonlinear optical probing and Raman spectroscopy of twisted h-BN tuned with MEGA2D. a**, Measurement scheme. A femtosecond laser at frequency  $\omega$  is focused onto the backside of a MEGA2D device through its fused silica substrate, and the reflected signal, part of which is at the frequency  $2\omega$ , is collected. At the focus are two pieces of h-BN crystal, one on the fused silica and the other on the MEMS pyramid tip. b, Measured SHG power in an h-BN MEGA2D device as a function of  $V_2$ . On the top axis, the corresponding separation between the two h-BN, h and the applied pressure after h reaches zero are shown. The red curve shows the calculated SHG power (Supplementary Information). **c**, A hysteresis is seen when bringing the two h-BNs in and out of contact. The amount of hysteresis, as converted to equivalent distance, is used to deduce the vdW interaction force (see main text). **d**, SHG power map of an as-fabricated

MEGA2D device. **e**, SHG power map when the h-BNs are brought into contact, which shows a possible bubble present in the middle of the pyramid top. **f**, On several rotations to  $\pm 10^\circ$  when engaged in contact, the bubble disappears and the SHG map appears more uniform. The square in **d**-**f** denotes the top surface of the pyramid, which is approximately  $4\times 4$  µm². **g**, An optical micrograph of the state in **f**. Scale bar, 5 µm. **h**, Measured second-harmonic circular dichroism, with  $(P_{\rm SHG}^{\circlearrowleft} - P_{\rm SHG}^{\circlearrowright})/(P_{\rm SHG}^{\circlearrowleft} + P_{\rm SHG}^{\circlearrowright})$ , where  $P_{\rm SHG}^{\circlearrowleft}$  and  $P_{\rm SHG}^{\circlearrowleft}$  are the SHG powers measured using LCP and RCP excitations, respectively. **i.j**, Raman spectroscopy of a MEGA2D h-BN sample when the twisted h-BN flakes are air-spaced by 0.8 µm (**i**) and in contact (**j**). Lines with different colours were taken at different twist angles. The dashed lines denote the centre of the  $E_{2g}$  peak fit with a Lorentzian.

To ensure hysteresis-free operation, we use electrostatic mechanisms for all actuators (Methods). Figure 1g shows the calculated actuation curve of the vertical actuator. The rotational actuator has a stepper motor design<sup>23</sup> with a step size of 0.33° and a range of  $\pm 10^\circ$ . The rotation axis is within about 1–2  $\mu$ m of the pyramid centre. Figure 1h shows the measured actuation curve of the rotator. Smaller steps are achievable by voltage interpolation.

The biggest advantage of MEGA2D is its flexibility. Apart from  $\theta$  and h, other interesting stacking parameters in 2DM, such as lateral translation, stretching, tilting and shearing, can be incorporated in the MEMS<sup>24–27</sup> (see Methods for tilting). There is also no limitation on the substrate material. This unlocks a variety of experiments, such as optics in 2DM, which we demonstrate below.

#### Moiré nonlinear optics

We measure the second-harmonic generation (SHG) in twisted h-BN single-crystals. 2DM with broken inversion symmetry, such as h-BN,

have a strong second-order nonlinear optical response ( $\chi^{(2)}$ ) that is highly sensitive to lattice orientation and stacking <sup>28–30</sup>. Further enhancement of the SHG signal can be achieved by the use of cavities <sup>31–33</sup>, plasmonic structures <sup>34</sup> and quasi-phase-matching <sup>7</sup>.

We first use SHG as a sensitive probe for h between the h-BN flakes. We assemble a MEGA2D device with an h-BN flake on the pyramid and another h-BN flake on a fused silica substrate. A  $\lambda$  = 780 nm femtosecond laser excites the h-BN through the fused silica substrate and the reflected SHG signal at  $\lambda/2$  = 390 nm is collected (Fig. 2a; see Methods for full setup). The h-BN flakes have thicknesses ranging from about 15 to 200 monolayers. Thick h-BN flakes can have nonzero SHG regardless of the parity of its number of layers because of electric quadrupole processes<sup>7</sup>.

We measure the SHG signal as a function of the vertical control voltage  $V_z$ , which tunes h (Fig. 2b). We find that SHG is tunable by more than an order of magnitude as a result of the Fabry–Pérot cavity formed by the two h-BN surfaces. It oscillates four periods before settling to a constant value, which indicates contact between the flakes. The cavity

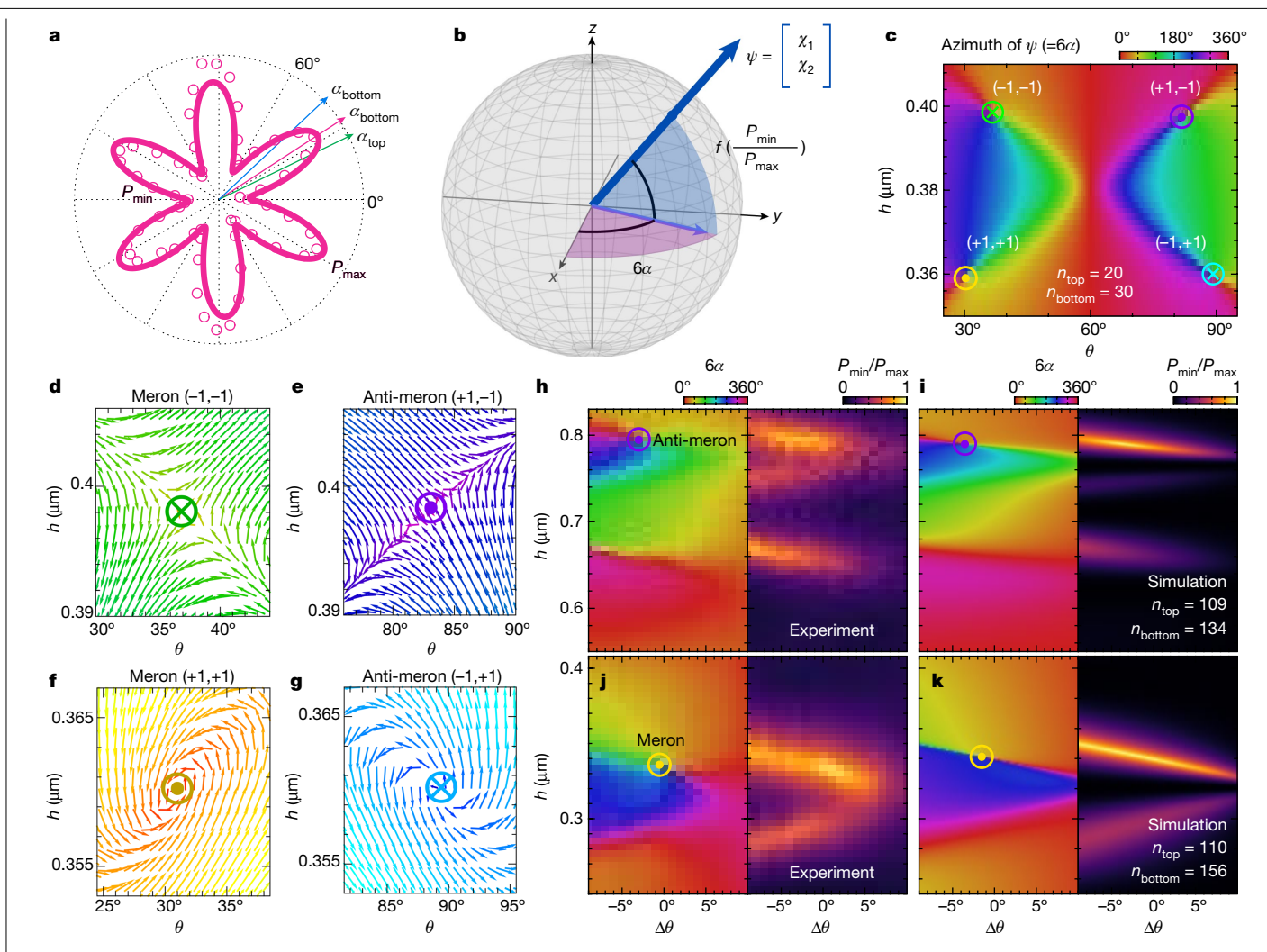


Fig. 3 | Experimental realization of synthetic merons (half-skyrmions) in the nonlinear susceptibility of twisted h-BN. a, A typical polarizationdependent SHG measurement in twisted h-BN. From each measurement, we can fit the SHG power to a cosine function with respect to the polarization to obtain three independent parameters: SHG power maxima  $P_{\text{max}}$ , minima  $P_{\min}$  and polarization  $\alpha$  of the maxima. The polarizations of maxima  $\alpha_{\text{top}}$  and  $\alpha_{\text{bottom}}$ , if only top or bottom h-BN is measured, are also shown. **b**, The effective nonlinear susceptibility of twisted h-BN, if written as a nonlinear pseudospin  $\psi$ , represents a direction on the Poincaré sphere. Its azimuth and elevation equal  $6\alpha$  and  $\pm 2 \tan^{-1}(P_{\min}/P_{\max})^{1/2}$ , respectively. The x-, y- and z-directions represent nonlinear pseudospins [1, 0],  $\frac{1}{\sqrt{2}}$ [1, 1] and  $\frac{1}{\sqrt{2}}$ [1, i], respectively. The function

 $f(x) = \pm 2 \tan^{-1}(x^{1/2})$ . The sign ambiguity is experimentally fixed by SHG CD (Methods).  $\mathbf{c}$ , Evolution of the azimuth  $6\alpha$  in the synthetic space for a system with  $n_{\text{top}} = 20$  and  $n_{\text{bottom}} = 30$ . In this space, we found four types of merons, labelled as (p, v) by their core polarity p and vorticity v.  $\mathbf{d} - \mathbf{g}$ , The pseudospin texture of the four types of merons in more detail. The product of p and vdefines the topological charge  $Q = p \times v$ , which equals +1 for a meron and -1 for an anti-meron. **h**, Experimentally measured  $6\alpha$  and  $P_{\min}/P_{\max}$ . **i**, The numerical simulation for a MEGA2D device, which exhibits a (+1, -1) anti-meron in the accessible synthetic space. The device has an initial twist of  $\theta = 43^{\circ}$  at  $\Delta\theta = 0^{\circ}$ . j,k, The experiment (j) and simulation (k) for a similar device that possesses a (+1, +1) meron instead.

enhancement is periodic in  $\lambda/2 = 390$  nm, and the observation thus matches well with the designed gap of about 1.6 μm.

The flatness of the mating interface is crucial for achieving a pristine 2D interface, which is maintained by the built-in mechanism discussed above. Figure 2d shows a typical SHG map of a free-standing device  $(h = 1.6 \mu m)$ . When the two flakes are brought into contact (Fig. 2e), we found that the SHG initially became non-uniform, which can be attributed to bubbles that formed between the flakes, as typically found during stacking of 2DM. However, on several rotations between ±10° while in contact, the SHG becomes more uniform (Fig. 2f), demonstrating the self-cleaning property of the 2D interface $^{6,35}$ .

MEGA2D also enables us to directly measure the mechanical properties of a 2D interface, such as the vdW attraction, traditionally measured by scanning probe techniques<sup>36,37</sup>. Figure 2c shows the SHG signal measured during forward and backward scanning of the vertical control voltage. We find a clear hysteresis on disengaging from contact, in

which the SHG suddenly jumps from the contact value, at h = 220 nm. Using the calculated MEMS vertical stiffness  $k_z = 300 \text{ N m}^{-1}$ , we estimate the maximum binding force  $F_b = k_z d = 66 \mu N$ , which corresponds to a vdW tensile strength of 4 MPa. This is comparable but smaller than the intrinsic cleavage strength of h-BN<sup>37</sup>, presumably because of the twist between the flakes.

H-BN crystals feature a mirror plane aligned with its armchair direction. For two h-BN twisted by  $\theta$  other than multiples of 60°, this symmetry is lifted by the emergent moiré pattern that imparts chirality, regardless of h. We can directly detect this breakdown in our experiment. Chiral materials respond differently to left (LCP) and right (RCP) circularly polarized light, as was demonstrated in twisted bilayer graphene<sup>38</sup>. To probe the chirality by SHG, we measure the SHG circular dichroism (CD) defined as  $(P_{SHG}^{\circlearrowleft} - P_{SHG}^{\circlearrowright})/(P_{SHG}^{\circlearrowleft} + P_{SHG}^{\circlearrowleft})$ , where  $P_{SHG}^{\circlearrowleft}$  and  $P_{SHG}^{\circlearrowleft}$  are the SHG powers excited using LCP and RCP, respectively. We purposefully fabricated a MEGA2D device with a free-standing twist

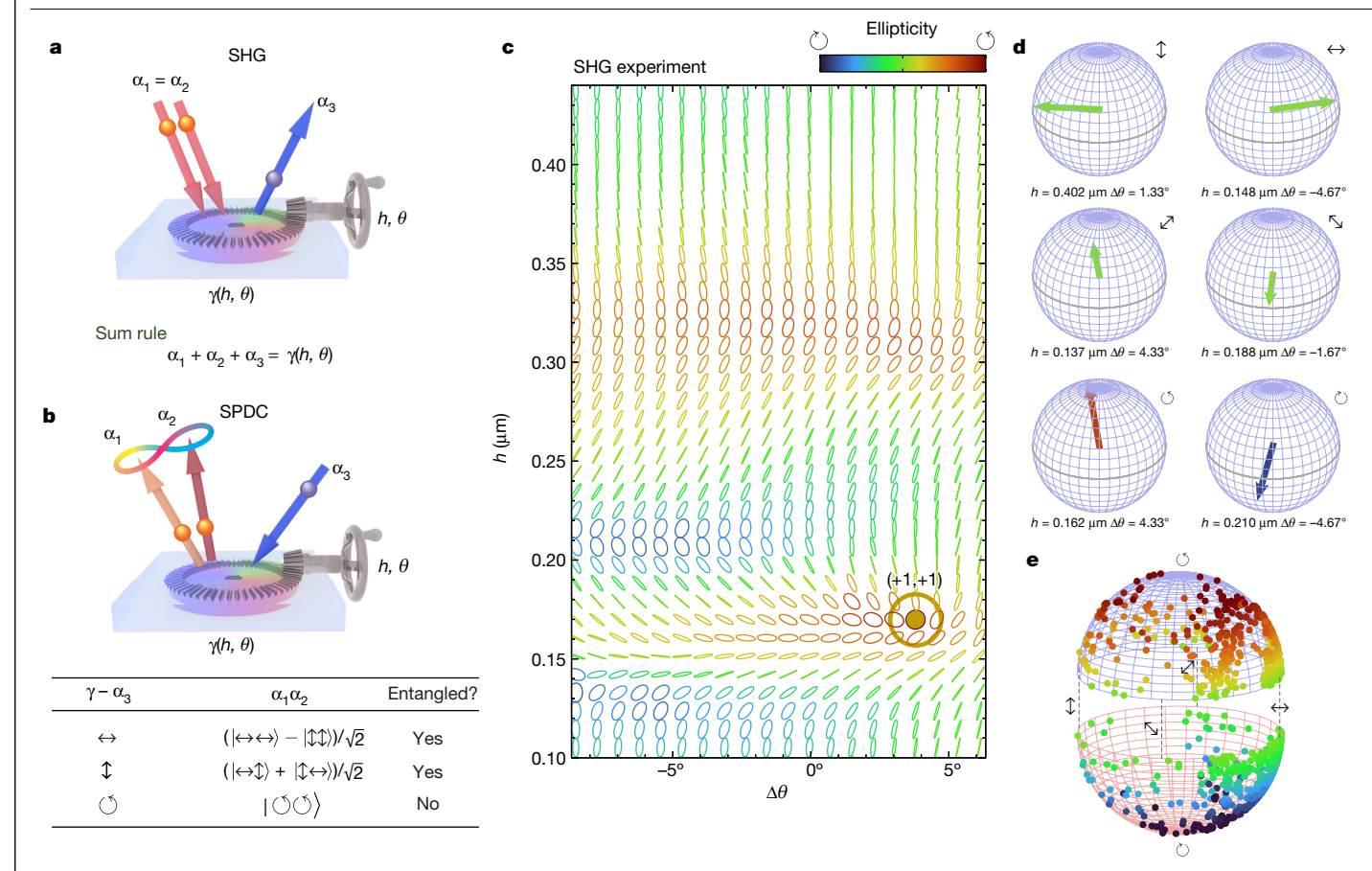


**Fig. 4** | **Tunable classical and quantum light source with MEGA2D.** Twisted h-BN has an intrinsic dimensionless complex number  $\gamma = \tan^{-1}(\chi_2/\chi_1)$  that characterizes its nonlinear susceptibility. **a**, In the SHG process, two photons with polarizations  $\alpha_1$  and  $\alpha_2$  (typically the same) combine into a photon with polarization  $\alpha_3$ . These angles obey a sum rule, such that  $\alpha_3$  can be controlled by  $\gamma$ , which is in turn tunable by  $\gamma$  and  $\gamma$ . In SPDC, which is the inverse process of SHG, the same sum rule is obeyed. However,  $\alpha_1$  can generally be different from  $\alpha_2$ , which results in an ambiguity. This ambiguity is related to the inherent quantum randomness of the SPDC process, and what we obtain is entangled photon pairs as shown in the table. The extent and direction of the entanglement

is tunable by  $\gamma$  and thus by h and  $\theta$ . Experimentally, we demonstrate only the SHG process here.  $\mathbf{c}$ , Demonstration of tunable SHG light source with MEGA2D. We show the measured  $\alpha_3$  as a function of h and  $\theta$ . Each ellipse in this plot represents a polarization state, with colour representing its ellipticity. The (+1, +1) synthetic meron located near the bottom right corner enables us to tune  $\alpha_3$  into left circular polarization.  $\mathbf{d}$ , The six main polarizations that we can access in this MEGA2D device.  $\mathbf{e}$ , The coverage of the Poincaré sphere. The upper and lower halves of the Poincaré sphere are split for clarity. The lower hemisphere shows less coverage because the accessible meron has p=+1.

angle near  $0^\circ$ . We can see from Fig. 2h that although the SHG CD varies strongly with h, it is always antisymmetric with  $\theta$  and vanishes at  $\theta = 0^\circ$ . We have thus demonstrated the ability to continuously vary the degree of symmetry breaking 'on-the-fly' using MEGA2D.

To further demonstrate the intimate contact between the 2DM when the vertical actuator is fully engaged, we measured the Raman spectroscopy of the twisted h-BN stack. The  $E_{2g}$  peak of h-BN centred around 1,365 cm<sup>-1</sup> caused by in-plane phonon modes is sensitive to stacking configuration and the layer number<sup>39,40</sup>. We find that the  $E_{2g}$  peak can shift by up to 0.6 cm<sup>-1</sup> when the h-BN flakes are brought into contact and twisted within  $\pm 8^{\circ}$  (Fig. 2i), whereas no shift is observed when the flakes are not in contact (Fig. 2j). We believe that it is the twist-dependent phononic coupling between the two h-BN flakes that is causing this shift.

# Topological texture in $\chi^{(2)}$

We can treat the stacking parameters offered by MEGA2D as synthetic dimensions  $^{8,9}$  to realize topological physics in the nonlinear properties of 2DM. In nonlinear optics involving 2DM, the second-order susceptibility  $\chi^{(2)}$  has eight components in the 2D plane. Materials with  $C_3$  crystallographic symmetry have two independent components:  $\chi_1 = \chi^{(2)}_{xxx} = -\chi^{(2)}_{yyy} = -\chi^{(2)}_{yxy} = -\chi^{(2)}_{yxy} = \chi^{(2)}_{xxy} = \chi^{(2)}_{xxy} = \chi^{(2)}_{xxy} = \chi^{(2)}_{yxx}$ . Other terms that contain the subscript z can in principle be excited

but do not contribute substantially in our scenario (Methods). We can write them as a pseudospin:  $\psi = [\chi_1, \chi_2]$ , representing a direction on the Poincaré sphere (Fig. 3b). For crystalline h-BN  $(D_{3h}$  symmetry),  $\psi \approx [1, 0]$  (x is armchair direction). For a generic stack of nonlinear 2DM, the effective  $\psi$  is a phase-coherent superposition of  $\psi$  from each constituent layer. In twisted h-BN, h and  $\theta$  control the SHG phase and polarization difference between the two flakes, respectively.  $\psi$  is periodic in both h (periodicity h2) and h4 (periodicity 120°), and the h6 synthetic space has the same torus-like topology as a 2D Brillouin zone.

Figure 3c shows the calculated azimuth map of  $\psi$  for  $n_{\rm top}$  = 20 layers of h-BN monolayers on fused silica and  $n_{\rm bottom}$  = 30 layers of h-BN monolayer on silicon, respectively. Rich features exist at certain locations in the synthetic space, around which the azimuth acquires full  $\pm 360^{\circ}$  rotations. These singularities are analogous to topological defects known as half-skyrmions or merons in magnetic materials  $^{10.41}$ . A meron is characterized by its topological charge  $Q = p \cdot v = \pm 1/2$ , determined by the core polarity  $p = \pm 1$  and the vorticity  $v = \pm 1$ ; p = +1 or -1 means that  $\psi$  points to +z or -z on the Poincaré sphere at the core, whereas v = +1 or -1 means that  $\psi$  forms a vortex or anti-vortex. In our system, we theoretically found all four types of synthetic merons (Q = +1/2) and anti-merons (Q = -1/2) (Fig. 3d–g).

With MEGA2D, we can access these topological features experimentally. To probe  $\psi$ , we measure the SHG power as a function of linear

polarization in a parallel configuration (Methods), yielding the characteristic six-fold symmetric pattern with respect to the polarization  $^{28-30}$  (Fig. 3a). We can identify the maximum and minimum SHG powers  $P_{\text{max}}$  and  $P_{\text{min}}$ , and the polarization of the maxima,  $\alpha$  (0° ≤  $6\alpha$  <  $360^{\circ}$ ), which are directly tied to the geometrical angles of  $\psi$  on the Poincaré sphere (Fig. 3b and Methods). In particular, when  $\psi$  is at the north or south pole,  $\alpha$  becomes undefined and  $P_{\text{min}}/P_{\text{max}}$  = 1, that is, the pattern in Fig. 3a becomes circular.

Figure 3h–k shows the measured and calculated  $6\alpha$  and ratio  $P_{\min}/P_{\max}$  in two MEGA2D devices. In one device (Fig. 3h,i), we can identify an anti-meron (Q=-1/2) labelled by (p,v) = (+1, -1). At its core,  $P_{\min}/P_{\max}$  approaches unity, consistent with the theoretical expectation. In the other device with different numbers of h-BN layers (Fig. 3j,k), we found a meron of the type (+1, +1) with similar behaviours. We note that p is not directly determinable by linear polarization SHG but can be separately identified by SHG CD (Methods).

# Towards a tunable quantum light source

These synthetic topological features imply that  $\chi^{(2)}$  of an active optical stack can be engineered to cover a large space, whereas h and  $\theta$  need to be tuned only slightly. We can use this advantage to design full-Stokes tunable classical and quantum light sources.

A second-order nonlinear process involves three photons with energies  $\hbar\omega_1$ ,  $\hbar\omega_2$  and  $\hbar\omega_3$ , where  $\hbar$  is the reduced Planck constant,  $\omega_1 + \omega_2 = \omega_3$  and polarizations are  $\alpha_1$ ,  $\alpha_2$  and  $\alpha_3$ , respectively. In a bulk nonlinear material, these polarizations typically need to be fixed on certain crystallographic planes to satisfy phase-matching requirements  $^{42}$ . In nonlinear 2DM, these requirements are relaxed, and the polarizations can be connected by a fourth polarization  $\gamma = \tan^{-1}(\chi_2/\chi_1)$ , by a sum rule (Methods)

$$\alpha_1 + \alpha_2 + \alpha_3 = \gamma + k_{\pi}, k = 0, \pm 1, \pm 2, \dots$$
 (1)

Here polarizations are represented by complex numbers with their real parts denoting their polarization angles and the imaginary parts encoding their ellipticity.

With y tunable by h and  $\theta$ , we realize a light source at frequency  $2\omega$ with tunable polarization state  $\alpha_3$ . In previous experiments in 2DM, active tuning of SHG polarization could be achieved only by intricate control of the arrival times of the two fundamental photons, and the tuning range was limited<sup>43</sup>. The tunability of  $\psi$  in our case can span the entire Poincaré sphere. We demonstrate this by fixing  $\alpha_1 = \alpha_2 = 0$  and measuring  $\alpha_3$  using quarter-wave plate polarimetry (Methods) in a MEGA2D device (Fig. 4c). We directly see the polarization vortex in  $\alpha_3$ at a synthetic meron, around which  $\alpha_3$  rotates by 180°. Exactly at the centre, the SHG becomes LCP ( $\alpha_3 = \gamma = +i\infty$ ). Figure 4d shows that all principal polarizations on the Poincaré sphere are approximately reached within the accessible synthetic space, and Fig. 4e shows the coverage on the sphere. Future generations of MEGA2D devices with a wider  $\theta$ range that allows access to a pair of merons with opposite polarity could provide better coverage of the sphere. The wide tunability of  $\psi$  can also potentially lead to new methods for generating spatiotemporal modulated light and quantum sensing of symmetry-breaking phenomena.

Another possibility using the same principles lies in the reciprocal process of SHG, known as spontaneous parametric down-conversion (SPDC)<sup>44</sup>, converting one photon at  $2\omega$  to two photons at  $\omega$ . Although SHG is fundamentally classical, SPDC is inherently quantum and can create entangled photon pairs with high purity. SPDC relies on the same  $\chi^{(2)}$  tensor, and the same sum rule (equation (1)) applies to the resulting photon pairs (Fig. 4b; see Methods for derivation). If  $\alpha_1 + \alpha_2 = \gamma - \alpha_3 = 0$ , we obtain a Bell's state  $(|\leftrightarrow\leftrightarrow\rangle - |\diamondsuit\uparrow\rangle)/\sqrt{2}$ . If  $\alpha_1 + \alpha_2 = \pi/2$ , we obtain another Bell's state  $(|\leftrightarrow\leftrightarrow\rangle + |\diamondsuit\leftrightarrow\rangle)/\sqrt{2}$ . If  $\gamma = +i\infty$  (that is,  $\psi \propto [1,i]$ , reachable at the core of a meron),  $\alpha_1$  and  $\alpha_2$  are both forced to be LCP, and the resulting photons have zero entanglement

The abilities of MEGA2D will speed up the exploration of the rich phase space of stacked 2DM and their applications. The nonlinear optics discussed in this Article is applicable to other  $\mathcal{C}_3$  monocrystalline thin films too. The MEMS-based technique can also be integrated with optical metamaterials and enable new ways to manipulate photons and to study light–matter interactions<sup>46</sup>.

#### **Online content**

Any methods, additional references, Nature Portfolio reporting summaries, source data, extended data, supplementary information, acknowledgements, peer review information; details of author contributions and competing interests; and statements of data and code availability are available at https://doi.org/10.1038/s41586-024-07826-x.

- Koren, E. et al. Coherent commensurate electronic states at the interface between misoriented graphene layers. Nat. Nanotechnol. 11, 752–757 (2016).
- Chari, T., Ribeiro-Palau, R., Dean, C. R. & Shepard, K. Resistivity of rotated graphitegraphene contacts. *Nano Lett.* 16, 4477–4482 (2016).
- Ribeiro-Palau, R. et al. Twistable electronics with dynamically rotatable heterostructures. Science 361, 690–693 (2018).
- Yang, Y. et al. In situ manipulation of van der Waals heterostructures for twistronics. Sci. Adv. 6, eabd3655 (2020).
- 5. Hu, C. et al. In-situ twistable bilayer graphene. Sci. Rep. 12, 204 (2022).
- 6. Inbar, A. et al. The quantum twisting microscope. Nature 614, 682-687 (2023).
- Yao, K. et al. Enhanced tunable second harmonic generation from twistable interfaces and vertical superlattices in boron nitride homostructures. Sci. Adv. 7, eabe8691 (2021).
- Yuan, L., Lin, Q., Xiao, M. & Fan, S. Synthetic dimension in photonics. Optica 5, 1396–1405 (2018).
- Ozawa, T. & Price, H. M. Topological quantum matter in synthetic dimensions. Nat. Rev. Phys. 1, 349–357 (2019).
- Göbel, B., Mertig, I. & Tretiakov, O. A. Beyond skyrmions: Review and perspectives of alternative magnetic quasiparticles. *Phys. Rep.* 895, 1–28 (2021).
- Novoselov, K. S., Mishchenko, A., Carvalho, A. & Neto, A. H. C. 2D materials and van der Waals heterostructures. Science 353, aac9439 (2016).
- Suárez Morell, E., Correa, J. D., Vargas, P., Pacheco, M. & Barticevic, Z. Flat bands in slightly twisted bilayer graphene: Tight-binding calculations. *Phys. Rev. B* 82, 121407 (2010).
- Bistritzer, R. & MacDonald, A. H. Moiré bands in twisted double-layer graphene. Proc. Natl Acad. Sci. USA 108, 12233–12237 (2011).
- Cao, Y. et al. Correlated insulator behaviour at half-filling in magic-angle graphene superlattices. Nature 556, 80–84 (2018).
- Cao, Y. et al. Unconventional superconductivity in magic-angle graphene superlattices. Nature 556, 43–50 (2018).
- 16. Andrei, E. Y. et al. The marvels of moiré materials. Nat. Rev. Mater. 6, 201-206 (2021).
- Mak, K. F. & Shan, J. Semiconductor moiré materials. Nat. Nanotechnol. 17, 686–695 (2022).
- 18. Liu, Y. et al. Van der Waals heterostructures and devices. Nat. Rev. Mater. 1, 16042 (2016).
- Meng, Y. et al. Photonic van der Waals integration from 2D materials to 3D nanomembranes. Nat. Rev. Mater. 8, 498–517 (2023).
- Lau, C. N., Bockrath, M. W., Mak, K. F. & Zhang, F. Reproducibility in the fabrication and physics of moiré materials. *Nature* 602, 41–50 (2022).
- Bell, D. J., Lu, T. J., Fleck, N. A. & Spearing, S. M. MEMS actuators and sensors: observations on their performance and selection for purpose. J. Micromech. Microeng. 15, S153 (2005).
- Algamili, A. S. et al. A review of actuation and sensing mechanisms in MEMS-based sensor devices. Nanoscale Res. Lett. 16, 16 (2021).
- Stranczl, M., Sarajlic, E., Fujita, H., Gijs, M. A. M. & Yamahata, C. High-angularrange electrostatic rotary stepper micromotors fabricated with SOI technology. J. Microelectromech. Syst. 21, 605–620 (2012).
- Cao, K. et al. Elastic straining of free-standing monolayer graphene. Nat. Commun. 11, 284 (2020).
- Zhang, Y., Gao, Y. & Xiao, D. Topological charge pumping in twisted bilayer graphene. Phys. Rev. B 101, 041410 (2020).
- Su, Y. & Lin, S.-Z. Topological sliding moiré heterostructure. Phys. Rev. B 101, 041113 (2020).
- Wang, G. et al. Recent advances in the mechanics of 2D materials. Int. J. Extrem. Manuf. 5, 032002 (2023).
- 28. Kumar, N. et al. Second harmonic microscopy of monolayer MoS<sub>2</sub>. *Phys. Rev. B* **87**, 161403 (2013)
- Malard, L. M., Alencar, T. V., Barboza, A. P. M., Mak, K. F. & de Paula, A. M. Observation of intense second harmonic generation from MoS₂ atomic crystals. Phys. Rev. B 87, 201401 (2013).
- 30. Li, Y. et al. Probing symmetry properties of few-layer  $MoS_2$  and h-BN by optical second-harmonic generation. *Nano Lett.* **13**, 3329–3333 (2013).

- Yi, F. et al. Optomechanical enhancement of doubly resonant 2D optical nonlinearity. Nano Lett. 16, 1631-1636 (2016)
- Day, J. K., Chung, M.-H., Lee, Y.-H. & Menon, V. M. Microcavity enhanced second harmonic generation in 2D MoS<sub>2</sub>. Opt. Mater. Express 6, 2360-2365 (2016).
- Fryett, T. K. et al. Silicon photonic crystal cavity enhanced second-harmonic generation from monolayer WSe2. 2D Mater. 4, 015031 (2016).
- Akselrod, G. M. et al. Leveraging nanocavity harmonics for control of optical processes in 2D semiconductors. Nano Lett. 15, 3578-3584 (2015).
- 35. Haigh, S. J. et al. Cross-sectional imaging of individual layers and buried interfaces of graphene-based heterostructures and superlattices. Nat. Mater. 11, 764-767 (2012).
- Lee, C., Wei, X., Kysar, J. W. & Hone, J. Measurement of the elastic properties and intrinsic strength of monolayer graphene. Science 321, 385-388 (2008).
- 37. Rokni, H. & Lu, W. Direct measurements of interfacial adhesion in 2D materials and van der Waals heterostructures in ambient air. Nat. Commun. 11. 5607 (2020).
- Kim, C.-J. et al. Chiral atomically thin films, Nat. Nanotechnol. 11, 520-524 (2016). 38.
- 39. Gorbachev, R. V. et al. Hunting for monolayer boron nitride: optical and Raman signatures. Small 7, 465-468 (2011).
- Krečmarová, M. et al. Optical contrast and Raman spectroscopy techniques applied to 40. few-layer 2D hexagonal boron nitride. Nanomaterials 9, 1047 (2019).
- 41. Guo, C., Xiao, M., Guo, Y., Yuan, L. & Fan, S. Meron spin textures in momentum space. Phys. Rev. Lett. 124, 106103 (2020).

- Guo, Q. et al. Ultrathin quantum light source with van der Waals NbOCl<sub>2</sub> crystal. Nature 613, 53-59 (2023)
- 43. Klimmer, S. et al. All-optical polarization and amplitude modulation of second-harmonic generation in atomically thin semiconductors. Nat. Photon. 15, 837-842 (2021).
- 44. Zhang, C., Huang, Y.-F., Liu, B.-H., Li, C.-F. & Guo, G.-C. Spontaneous parametric down-conversion sources for multiphoton experiments. Adv. Quant. Technol. 4, 2000132
- 45. Shi, J. et al. 3R MoS<sub>2</sub> with broken inversion symmetry: a promising ultrathin nonlinear optical device. Adv. Mater. 29, 1701486 (2017).
- Tang, H. et al. Experimental probe of twist angle-dependent band structure of on-chip optical bilayer photonic crystal. Sci. Adv. 9, eadh8498 (2023).

Publisher's note Springer Nature remains neutral with regard to jurisdictional claims in published maps and institutional affiliations.

 $Springer\ Nature\ or\ its\ licensor\ (e.g.\ a\ society\ or\ other\ partner)\ holds\ exclusive\ rights\ to\ this$ article under a publishing agreement with the author(s) or other rightsholder(s); author self-archiving of the accepted manuscript version of this article is solely governed by the terms of such publishing agreement and applicable law.

© The Author(s), under exclusive licence to Springer Nature Limited 2024

## **Methods**

#### MEMS working principle

The core of the on-chip MEGA2D platform is the MEMS die in which 2D material resides. Here we briefly outline the working principle of the MEMS device and the fabrication procedure.

MEMS actuators that are commonly used in research and commercial products are broadly classified into electrostatic, piezoelectric and thermal actuators. Each category has different advantages and disadvantages. Among them, electrostatic actuators are the only ones that offer fast response, zero backlash (hysteresis) and compatibility with the widest operating environment. Compared with piezoelectric actuators, which typically have a small percentage of deformation, nonnegligible hysteresis and expansion and contraction due to changes in temperature and magnetic field, the electrostatic actuator is much more friendly for on-chip integration of 2D materials.

The basic working principle of electrostatic actuators relies on a parallel-plate capacitor. The energy of a parallel-plate capacitor in a vacuum is

$$E = \frac{1}{2}CV^2 = \frac{\varepsilon_0 A V^2}{2d},\tag{2}$$

where C is capacitance, V is voltage on the capacitor,  $\varepsilon_0$  is vacuum permittivity, A is the area of overlap and d is the distance between the plates. We assume the width of the capacitor w is much larger than d and ignore any edge effects. If a capacitor has a fixed plate and a movable plate that can displace perpendicularly (towards the other plate, which we call z-direction), as well as parallelly (which we call x-direction), the electrostatic forces are

$$f_z = \frac{\mathrm{d}E}{\mathrm{d}z} = -\frac{\varepsilon_0 A V^2}{d^2},\tag{3}$$

$$f_x = \frac{dE}{dx} = \frac{\varepsilon_0 l V^2}{d},\tag{4}$$

where l is the extent of the capacitor in the y-direction, and A = wl. A MEMS electrostatic actuator essentially uses one of these two forces to balance the reaction force of a MEMS spring (simply modelled by Hooke's law  $f = k\delta$ , where k is the spring constant) to achieve a voltage-controlled displacement  $\delta = f/k$ . Notably, the vertical actuation force is typically larger than the parallel actuation force, as w is typically larger than d. The drawback of vertical actuation, however, is that there is a pull-in instability that limits the maximum displacement to about d/3.

Our MEMS device consists of a rotator (R) stage cascaded on the vertical stage (Z). The Z stage uses the perpendicular force equation (3). As mentioned above, this type of actuator can provide large forces but has a limited range. We devised a lever-based mechanism to amplify the motion (Extended Data Fig. 1a,b). The resulting actuator can provide up to 5 µm of motion when actuated to around 50 V. We put mechanical limiters on the levers to prevent shock damage and electrostatic pull-in.

By contrast, the R stage uses the actuation force from equation (4). To achieve considerable motion with this smaller force, we note that equation (4) is independent of the dimension of the capacitor along the motion (w). It is therefore desirable to break the capacitor into as many smaller capacitors as possible (until  $w \approx d$ ). We end up either in a 'comb' design or a 'teeth' design. The latter is more suitable for rotary motion, as we can construct actuator teeth around the rotary core to create a stepper motor without sacrificing force for range<sup>23</sup>. The design of the R stage is shown in Extended Data Fig. 1c. For continuous rotation, the teeth are split into three groups that are shifted a third of a tooth from each other (Extended Data Fig. 1d).

To cascade the R stage on top of the Z stage, we designed an interstage electrical network with vias to connect the control voltages of the R stage. Proper design of this network ensures that there is minimal crosstalk between the Z and R stages.

#### **MEMS fabrication**

The MEMS die is fabricated from a commercial silicon-on-insulator wafer and contains no metal or polymer. The die is thus extremely robust against heat, refrigeration or magnetic fields. The fabrication procedure is outlined in Extended Data Fig. 2. The main processing steps are

- tip etching,
- through-silicon vias (TSV) fabrication,
- MEMS structure etching and release and
- bonding.

**Tip etching.** We start with a 6-inch silicon-on-insulator wafer, consisting of a 450-μm Si handle layer, a 2-μm buried oxide (BOX) layer and a 60-μm Si device layer. Each wafer contains 332 dies. The wafer is first coated with thermally grown silicon dioxide on both sides (Extended Data Fig. 2a). On the back side of the wafer (Si handle), the oxide is etched into a small square (Extended Data Fig. 2b). The underlying silicon layer is etched into a pyramid (either sharp or flat-top) using a 45% potassium hydroxide solution at 75 °C. The height of the pyramid is controlled by etching time to be around 600 nm. The oxide mask is subsequently removed in a dilute hydrofluoric acid (HF) solution (Extended Data Fig. 2c).

**TSV fabrication.** The TSVs act as electrical connections between top and bottom p-doped silicon layers. The TSVs are first patterned on the device layer by photolithography on a thick photoresist. The device layer and the BOX layer are subsequently removed by reactive-ion etching. The wafer is thoroughly cleaned to remove etching residues. A conductive layer, for example, poly-silicon, is conformally deposited on the wafer, ensuring full coverage of the TSVs. To protect the back side of the wafer from deposition, an oxide film is grown with plasma-enhanced chemical vapour deposition. This oxide and the poly-silicon on it are removed by reactive-ion etching before proceeding (Extended Data Fig. 2d).

MEMS structure etching and release. This fabrication step comprises three steps: backside patterning, front side patterning and HF release (Extended Data Fig. 2e). A tetraethylorthosilicate oxide mask is first grown on both sides of the wafer. The Si handle layer is patterned and etched from the bottom up to the BOX layer, using deep reactive-ion etching. After plasma cleaning, the front side is then patterned and etched from the front side down to the BOX layer. At this stage, the wafer becomes fragile and must be handled with extreme care. The final stage is the HF release. The wafer is thoroughly cleaned to remove fluorocarbon residue. The BOX layer, as well as the remnant oxide mask, is etched using an HF vapour etcher (AMMT GmbH) at 35 °C for 45 min. This step releases the MEMS actuators and suspends the Si pillar. We used a dicing-free design such that the wafers are automatically released into chips without the need for saw-cutting<sup>47</sup>.

**Bottom chip fabrication and bonding.** The bottom chip is fabricated from a fused silica wafer pre-patterned with alignment markers. After the 2DM flakes are transferred, a 2.2- $\mu$ m thick SU-8 layer is patterned on the wafer. The fused silica wafer is then diced using a commercial dicing saw into  $1\times1$  cm² chips. Each MEMS die is aligned to a fused silica chip and bonded using heat and pressure (Extended Data Fig. 2f) to become a complete MEGA2D device. Finally, each device is electrically connected to a measurement printed circuit board by wire bonding.

**2DM transfer.** To transfer flakes of 2DM onto the MEMS pyramid without damaging the suspended MEMS structures, which is susceptible to shock and stiction if exposed to liquid, we developed a modified

dry transfer method using poly(bisphenol A carbonate) (PC) film. We prepare thin PC and polypropylene carbonate (PPC) film by spin coating on a clean Si wafer and stack them on a pre-moulded polydimethylsiloxane (PDMS) flat-top pyramid (the tip diameter is 500 μm). We stack the PC on top of the PPC before putting them down onto the PDMS pyramid, to provide a thermal releasing mechanism at 200 °C, at which temperature the PPC has completely melted. The higher tackiness of the PC facilitates the pick-up of 2DM. We first pick up h-BN flakes at 70-90 °C 40-μm-tall ridges etched on a Si wafer to cut the PC/PPC stack at 180 °C into a small square. This step makes it easier to release the PC/PPC stack onto the MEMS Sipillar. The segregated PC/PPC square with h-BN flake is released on the MEMS Si pillar at 200 °C. The PC and PPC are removed in chloroform in a special holder that prevents the solvent from entering the active MEMS structure because any liquid in the MEMS will cause stiction. The MEMS die is subsequently annealed in a vacuum at 300-500 °C overnight to remove the PC and PPC residue. Extended Data Fig. 3 shows an h-BN flake before and after the transfer.

A simpler procedure is performed on the fused silica substrate side. We use a PC/PDMS stack to pick up the h-BN at similar temperatures as above and directly release it onto a clean fused silica substrate at 150 °C. SU-8 is subsequently spun and patterned on the substrate. The substrate is then cut with a dicing saw into 1 × 1 cm² chips. The assembly of the MEMS chip and fused silica substrate takes place at 200 °C, which activates the SU-8 and forms a strong bond between the two chips. Cleanliness of the fused silica and MEMS chips is crucial to the success, which means any dust that is larger than a few microns must be removed. In all the steps described above, we take note of the orientation of the h-BN flakes that was pre-determined by SHG measurement and use that information to align the h-BN flakes to be within about 2°.

We demonstrate the abilities of the MEGA2D platform mainly using SHG. The SHG response to different polarized light is measured in a reflectance setup as shown in Extended Data Fig. 4a. The light source is a 780-nm femtosecond fibre laser with a nominal pulse width of about 100 fs. After rotating the polarization using a  $\lambda/2$  plate and optionally a  $\lambda/4$  plate (for SHG CD measurements), the light beam is focused onto the MEGA2D sample from the fused silica side using a 40× objective. The reflected SHG light is collected with the same objective, goes back through the same waveplates and is separated from the incident beam using a dichroic mirror. This reflected beam is further filtered by a bandpass filter to remove the fundamental light, passed through a linear polarizer (set to be parallel with incident laser polarization) and measured by a custom-made camera spectrometer.

We also use quarter-wave plate (QWP) polarimetry to measure the polarization of the reflected SHG wave directly. The modified setup is shown in Extended Data Fig. 4b. The fundamental polarization is fixed to vertical in this case. The polarizer is also fixed to pass vertical polarization. The SHG signal is measured as a function of the QWP angle  $\theta$  when it is rotated from 0° to 180°. This information is used to extract the Stokes parameters  $S_0$ ,  $S_1$ ,  $S_2$  and  $S_3$  of the SHG light<sup>48</sup>. The Stokes parameters are normalized with respect to  $\sqrt{S_1^2 + S_2^2 + S_3^2}$  and plotted either as polarization ellipses or on the Poincaré sphere (Fig. 4).

The Raman spectroscopy in Fig. 2i, j is performed in a commercial Horiba Raman spectrometer at room temperature, using a 532-nm laser excitation, an excitation power of 10 mW and an integration time of 30 s.

Supplementary Video 1 shows the in situ twisting of two pieces of h-BN under an optical microscope.

#### Theory of SHG and SPDC in twisted h-BN

See Supplementary Information for details.

## Experimental data post-processing

The raw experimental data (SHG versus h, SHG CD,  $\alpha$  and  $P_{min}/P_{max}$  maps, and polarization map) are all measured as functions of  $V_{zz}$  the MEMS

vertical actuation voltage. We first need to convert  $V_z$  into h. The nominal dependence of h on  $V_z$  is shown in Fig. 1, and the MEGA2D devices from the same batch typically do not deviate from this curve considerably. The small deviation can be corrected by a simple scaling factor on h. This factor is fit from the SHG versus h measurement (Fig. 2b), because the distance between the periodic peaks must be equal to  $\lambda/2$ . Accuracy of h calibration is, therefore, dependent on precise knowledge of the fundamental wavelength  $\lambda$ , which is from the ultrafast fibre laser we use for pumping and is stable at 780 nm.

Despite our best efforts, there is a small crosstalk between the Z and R stages, which results in a quadratic drift of vertical position with respect to  $\theta$ , that is, there is a drift in the form of

$$\Delta h \propto (\theta - \theta_0)^2$$
,

where  $\theta_0$  is a constant. We fit our measurement data with this formula to remove the quadratic background. Extended Data Fig. 5 shows a comparison between the raw and corrected SHG CD data as an example.

Experimental data in Figs. 2h, 3h, j and 4c and Extended Data Figs. 5 and 6 are interpolated into a rectangular grid of the same resolution as the raw data for the purpose of plotting. Figure 4d,e shows the raw data points corresponding to Fig. 4c without any interpolation.

#### Additional SHG CD simulation and experiment data

Extended Data Fig. 6a shows the simulated SHG CD corresponding to Fig. 2h. The number of layers of the top and bottom h-BN is  $n_{\rm top}$  = 39 and  $n_{\rm bottom}$  = 190.

Extended Data Fig. 6b,c shows the measured SHG CD data at the meron and anti-meron shown in Fig. 3h–k. Although measuring  $\alpha$  and  $P_{\min}/P_{\max}$  alone cannot pinpoint the polarity p of the meron and anti-meron, the polarity of the SHG CD data help us to unambiguously identify p=1 for both the anti-meron and meron shown in Fig. 3h–k.

#### Other nonlinear responses allowed by $C_3$ symmetry

Apart from  $\chi_{xxxx}$ ,  $\chi_{yyyy}$  and the terms derived from them,  $C_3$  symmetry allows several other nonzero terms in a rank-3  $\chi^{(2)}$  tensor, including  $\chi_{xxxx}$ ,  $\chi_{yyz}$ ,  $\chi_{xyz}$  and  $\chi_{zzz}$  and their permutations. All these terms require an electric field along the z-direction (perpendicular to the 2DM) to excite. In SHG experiments on twisted bilayer graphene, it was shown that the interfacial effects can greatly enhance  $\chi_{xyz}$ , which could be observed in a setup using large numerical aperture (NA) pumping (NA  $\approx$  0.9). As graphene does not have an intrinsic  $\chi_{xxx}$  response, the interfacial  $\chi_{xyz}$  can be large and dominate the observed SHG polarization pattern. The observed SHG polarization pattern can become three-fold symmetric when both  $\chi_{xxx}$  and  $\chi_{xyz}$  are present.

In our experiment, we used an NA  $\approx 0.25$  and at a wavelength of 780 nm, the Rayleigh range is about 4  $\mu$ m for a Gaussian laser beam. Therefore, even at the largest MEMS separation  $h=1.6~\mu$ m, the entire air-spaced h-BN stack sits within a small fraction of the Rayleigh range from the beam waist. In these conditions, the electromagnetic field has only a tiny fraction out of plane. Using the estimation from literature<sup>49</sup>, the out-of-plane electric field is at most 1% of the total field. We can arbitrarily create a large out-of-plane electric field by oblique pumping<sup>50</sup>, but we have used perpendicular pumping in all our experiments. In these conditions, any effect of  $\chi_{xyz}$  (or  $\chi_{xxz}$ ,  $\chi_{yyz}$ ) is at least 100 times smaller than the effect of  $\chi_{xxx}$  or  $\chi_{yyy}$ .

As h-BN does not have an intrinsic  $\chi_{xyz}$  but does have a large intrinsic  $\chi_{xxx}$ , we believe the combined result is that any appreciable SHG we observe in our experiments originates from the  $\chi_{xxx}$  and  $\chi_{yyy}$  terms, that is, the nonlinear pseudospin we introduced. We also do not observe a three-fold SHG pattern in our experiments accordingly.

We note that if the pump beam is not Gaussian, however, a much larger fraction of the electric field can become out of plane at the beam waist. Pumping the twisted h-BN system with such a spatially

modulated light source—for example, a vortex light with orbital angular momentum—could be exploited to engineer even more versatile tunable light sources that use  $\chi_{xyz}$ .

We also note that the  $C_3$  symmetry, which is inherent to h-BN or many TMDs, implies the well-known SHG selectivity rule: LCP excitation generates RCP SHG light only, and vice versa. This could be directly captured in our sum rule formula, by setting  $\alpha_1=\alpha_2=+\mathrm{i}\infty$  (corresponding to LCP). For any value of  $\gamma$ , the only possible solution is  $\alpha_3=-\mathrm{i}\infty$ , which means an RCP SHG output. We note that this selectivity is different from the SHG CD we measured. Although LCP fundamental generates only RCP SHG and vice versa, these two processes can have different rates if the system breaks chiral symmetry (that is, lowering from  $D_{3\mathrm{h}}$  to  $C_3$ ). The in situ breaking of this chiral symmetry is shown in Fig. 2h.

#### Interfacial flatness, parallelism and strain profile of MEGA2D

To achieve an intimate 2D contact, it is crucial that the two mating flakes in the MEGA2D are flat and parallel, and the strain profile of the flake on the Si pyramid is controlled.

The flatness of the 2DM in a MEGA2D device is guaranteed by the intrinsic flatness of the underlying substrate, that is, the fused silica substrate and the Si pyramid. Extended Data Fig. 7a shows the AFM line scan of an h-BN flake on the Si pyramid. It can be seen that the h-BN flake is extremely flat with an average roughness (Ra) of 0.11 nm, and the maximum deviation over a 4- $\mu$ m baseline is less than 0.5 nm.

The parallelism between the two flakes in a MEGA2D device can be estimated by a few simple experiments. Extended Data Fig. 7b shows the AFM line scan across the Si pyramid over the Si pillar (Fig. 1e). We can see that the baseline of the Si pyramid is essentially parallel to the Si pillar surface. Therefore, as it is difficult to check the parallelism of the mating interfaces of MEGA2D directly, we can use the Si pillar as a reference to determine whether it is parallel to the fused silica substrate.

The air gap between the Si pillar and fused silica substrate displays a characteristic colour because of interference, when viewed under a white-light microscope. If the two surfaces are tilted, it displays coloured stripes (that is, Newton rings). This allows us to determine the distance variation between the two surfaces with precision down to a fraction of the visible light wavelength. Extended Data Fig. 7c,d shows the optical images (colour saturated) of a normal and a defective MEGA2D device, respectively. The defective device has a dust particle at one corner of the SU-8 spacer. The defective device displays coloured stripes, whereas the normal device does not. We performed a simple TMM calculation to simulate the colour of a SiO<sub>2</sub>-air-Si stack under white-light illumination. From the simulation (Extended Data Fig. 7e, f), we can easily detect a tilt angle of 0.01° using this technique. Therefore, the fact that we did not see any clear coloured stripes indicates that the Si pillar, and by extension the Si pyramid, is parallel within 0.01° with the fused silica substrate.

The MEGA2D device further provides a built-in mechanism to compensate for this level of remnant tilt angle, which might result when a temperature or magnetic field gradient exists. The MEMS vertical actuator consists of four quadrants, each of which can be driven independently. For pure vertical movements, they are tied to the same voltage  $V_z$ . To achieve tilting, we can apply different voltages to them. For example, as shown in Extended Data Fig. 7g, applying 60 V to the top-side actuators while applying zero voltage to the bottom-side actuators causes the Si pillar to tilt towards the y-direction. Similarly, applying a voltage to the right side but not the left side actuators causes the Si pillar to tilt towards the x-direction (Extended Data Fig. 7h). The maximum tilt that can be achieved this way is approximately 0.008°, and tilting in x- and y-directions can be combined to achieve a tilt along any direction.

We further perform an experiment to check the strain of the h-BN flake after it is transferred onto the Si pyramid. We first perform pre-patterning of an h-BN flake by e-beam lithography and a short reactive-ion etching to create a precise array of holes with a spacing

of 250 nm and a diameter of about 50 nm. After transferring the flake to the Si pyramid, we clean the flake and perform AFM to accurately determine the new positions of the holes. If there is an in-plane strain on the flake, it can be extracted from the change in spacing between the holes (Extended Data Fig. 7i). After extracting the hole spacing, we use a median filter to calculate a smoothly varying strain profile.

We measured two samples, and their strain profiles are shown in Extended Data Fig. 7j,k. We showed only the strain component  $\varepsilon_{xx}$  here because the determination of the *y*-spacing between the holes is subject to AFM artefacts, distortion and drifting, and thus is less accurate. We find that the strain within the pyramid region (denoted by red dashed lines) is of the level of 0.2%, whereas outside the pyramid region, it can reach up to 0.5%. Therefore, h-BN flakes transferred to Si pyramids have low residual strain on top of the pyramid.

Although beyond the scope of the current work, we would also like to briefly comment on the strain profile when there are other 2DM on top of the h-BN, for example, monolayer graphene or TMDs, for other types of measurements. We note that in a multilayer system such as this, there could be additional strain or strain gradient between the h-BN and the graphene/TMD above it. We believe that there are simple methods for mitigating these unwanted effects. For example, we can 'pin' the graphene/TMD layer to the h-BN by reactive-ion etching slightly outside the region above the Si pyramid. Some pinning effect can also be achieved by pre-annealing the h-BN/graphene stack<sup>3,51</sup>. Once the graphene/TMD is pinned with the h-BN, its strain profile can be well controlled and optimized, as shown above. Moreover, local strain always exists in twisted devices, even those made using conventional stacking methods, because of the interatomic interactions and lattice relaxation that are extremely strong. Although putting an exfoliated layer on the Si pyramid might introduce a small amount of additional strain, when the two surfaces are in contact this strong atomic interaction will locally dominate to produce a strain field that is comparable to the existing devices.

For future experiments that involve, for example, a monolayer graphene layer on h-BN, further study is needed to determine whether twisting in situ could change the strain profile. It was demonstrated very recently that sa standalone graphene can be strained by rotating a small piece of h-BN on top of it, by up to 2.5% in strain and 1° µm<sup>-1</sup> of twist angle gradient. Compared with this demonstration, which uses a long and narrow strip of graphene, the 2DM (for example, monolayer graphene) on our Si pyramid has an aspect ratio of 1:1, fully supported from all sides, and should, therefore, be much more rigid in-plane. We thus believe that it should be much more stable against in-plane twist disorder and strain gradient. The mechanical stability of 2DM transferred on a pyramid is further supported by the demonstration in ref. 6, albeit the MEGA2D has a slightly larger area of contact between the 2DM compared with this demonstration.

# **SPDC** efficiency

We notice that the SPDC photon count is linearly dependent on the pump power, so local enhancement of the electrical field at the 2DM (for example, 3-R MoS<sub>2</sub>, r-BN) has a direct enhancement on the overall SPDC conversion efficiency. This could be achieved with nanophotonic structures, where Q-factor (and thus enhancement factor) more than  $10^7$  can be expected theoretically<sup>53</sup>. As tunable SPDC requires only enhancement at a single wavelength, this type of photonic crystal cavity can be readily designed and integrated, either on the substrate or etched onto the nonlinear 2DM with a thickness equal to the coherence length.

A different approach to achieving a sizable SPDC efficiency while retaining all the entanglement tunability is to use patterned nonlinear metasurfaces in place of nonlinear 2DM. Metasurfaces can use materials, such as LiNbO<sub>3</sub> and GaAs, with high  $\chi^{(2)}$ , and the resonant nanostructures can further enhance SPDC by several orders of magnitude <sup>54,55</sup>. Higher-Q photonic structures, for example, those involving

bound-state in-continuum, could be used for this improvement. To keep all the tunability of a  $C_3$  2DM, especially retaining the nonlinear pseudospin physics and the sum rule we introduced, it is possible to use a metasurface design that has  $C_3$ -symmetric unit cells, following a recent demonstration that this type of metasurface can generate tunable SHG that follows a similar sum rule as  $C_3$ -symmetric 2DM<sup>56</sup>. We have also shown recently that this photonic structure can be seamlessly integrated with our MEGA2D platform (in a modified arrangement)<sup>57</sup>.

#### Additional comments

As we demonstrated above, our MEGA2D platform can tilt by a small amount in both x- and y-directions to compensate for the possible tilt angles caused by the temperature or magnetic field changes. This tilting, combined with our ability to apply pressure, can, in principle, be used to compensate for a small heterogeneity in twist angle in certain systems, such as twisted bilayer graphene, because changing the local pressure has a similar effect as changing the local twist angle in this system  $^{58}$ . Although the optical experiments demonstrated in this work do not require these capabilities, it is certainly interesting to compensate, or to even engineer, an effective twist–pressure gradient in future experiments using the tilting mechanism.

We also note that in our MEGA2D system, the two-dimensional material does not lock up to commensurate/aligned angles (that is,  $0^{\circ}$ ,  $60^{\circ}$ ,  $120^{\circ}$ ), as was observed previously³. We have purposefully designed the MEGA2D platform from the very first design to avoid the locking effect from occurring to avoid sudden jumps when changing the twist angle so that high accuracy and repeatability in twisting can be achieved. There are two reasons why the locking cannot happen in our design: (1) As the two-dimensional material on the Si pyramid is tented, the part of the two-dimensional material on the Si pyramid is rigidly connected to the part of the two-dimensional material on the Si pillar that does not touch the two-dimensional material on the substrate. Therefore, even if locking occurs, this added rigidity helps to unlock the 2D interface that is in contact (at most  $4\times4~\mu\text{m}^2$ ). (2) The MEMS rotational spring is stiff enough to provide the torque necessary to unlock the interface.

Although the MEGA2D technology does not eliminate the reproducibility issue, we wish to emphasize that the additional reproducibility of MEGA2D comes from the fact that only a single device is necessary to explore a wide range of parameter space. Therefore, although the assembly of MEGA2D devices still uses a dry transfer method, MEGA2D can already increase the reproducibility by at least 5–10 times (assuming that 5–10 conventional 2DM devices are necessary to explore the same parameter space, which is, in our experience, far from being enough). We predict that the reproducibility could be further enhanced if the 2DM of interest can be directly grown on the Si pyramid of the MEGA2D device, for example, by chemical vapour deposition, epitaxy or other scalable methods.

## **Data availability**

All relevant data presented in this paper can be found in the data repository at https://doi.org/10.7910/DVN/UTIAOK.

- Sari, I., Zeimpekis, I. & Kraft, M. A dicing free SOI process for MEMS devices. Microelectron. Eng. 95, 121–129 (2012).
- 48. Collett, E. Polarized Light: Fundamentals and Applications (Marcel Dekker, 1993).
- Yang, F. et al. Tunable second harmonic generation in twisted bilayer. Graphene. Matter 3, 1361–1376 (2020).
- Kim, B. et al. Three-dimensional nonlinear optical materials from twisted two-dimensional van der Waals interfaces. Nat. Photon. 18, 91–98 (2024).
- Wang, W. et al. Evidence for an edge supercurrent in the Weyl superconductor MoTe<sub>2</sub>. Science 368, 534–537 (2020).
- Kapfer, M. et al. Programming twist angle and strain profiles in 2D materials. Science 381, 677-681 (2023)
- Ning, T., Zhao, L., Huo, Y., Cai, Y. & Ren, Y. Giant enhancement of second harmonic generation from monolayer 2D materials placed on photonic moiré superlattice. *Nanophotonics* 12, 4009–4016 (2023).
- Santiago-Cruz, T. et al. Photon pairs from resonant metasurfaces. Nano Lett. 21, 4423–4429 (2021).
- Zhang, J. et al. Spatially entangled photon pairs from lithium niobate nonlocal metasurfaces. Sci. Adv. 8, eabq4240 (2022).
- Wang, H. et al. All-optical ultrafast polarization switching with nonlinear plasmonic metasurfaces. Sci. Adv. 10. eadk3882 (2024).
- Tang, H. et al. On-chip multidimensional dynamic control of twisted moiré photonic crystal for smart sensing and imaging. Preprint at https://doi.org/10.48550/arXiv.2312. 09089 (2023).
- Yankowitz, M. et al. Tuning superconductivity in twisted bilayer graphene. Science 363, 1059–1064 (2019).

Acknowledgements We thank M. Zhang, B. Lou and G. Zhong for their helpful discussions. E.M. acknowledges support from the National Science Foundation (NSF) under contract CCS-2234513 and the DARPA under contract URFAO: GRS10802. A.Y. acknowledges support from the Army Research Office (grant no. W911NF-21-2-0147) and the Gordon and Betty Moore Foundation (grant no. GBMF 9468). S.F. acknowledges the support of a MURI grant from the US Air Force Office of Scientific Research (grant no. FA9550-21-1-0312). The sample fabrication was performed at the Harvard University Center for Nanoscale Systems, which is a member of the National Nanotechnology Coordinated Infrastructure Network and is supported by the NSF (award no. 1541959). K.W. and T.T. acknowledge support from the Elemental Strategy Initiative conducted by the MEXT, Japan (grant no. JPMXP0112101001), JSPS KAKENHI (grant no. JP20H00354) and the CREST (JPMJCR15F3), JST. P.J.-H. acknowledges support from the NSF (DMR-1809802), the STC Center for Integrated Quantum Materials (NSF grant no. DMR-1231319), the EPiQS Initiative of the Gordon and Betty Moore Foundation (grant GBMF9463), the Fundación Ramon Areces and the CIFAR Quantum Materials programme.

**Author contributions** Y.C. and A.Y. conceived the experimental ideas. Y.C. designed the MEGAZD platform. H.T., Y.W. and Y.C. performed the sample fabrication. H.T., E.M. and Y.C. performed the optical measurements. K.W. and T.T. provided the h-BN crystals. X.N., S.F. and Y.C. developed the theory. S.F. and P.J.-H. provided insightful discussions. H.T. and Y.C. wrote the paper with input from all authors.

Competing interests The authors declare no competing interests.

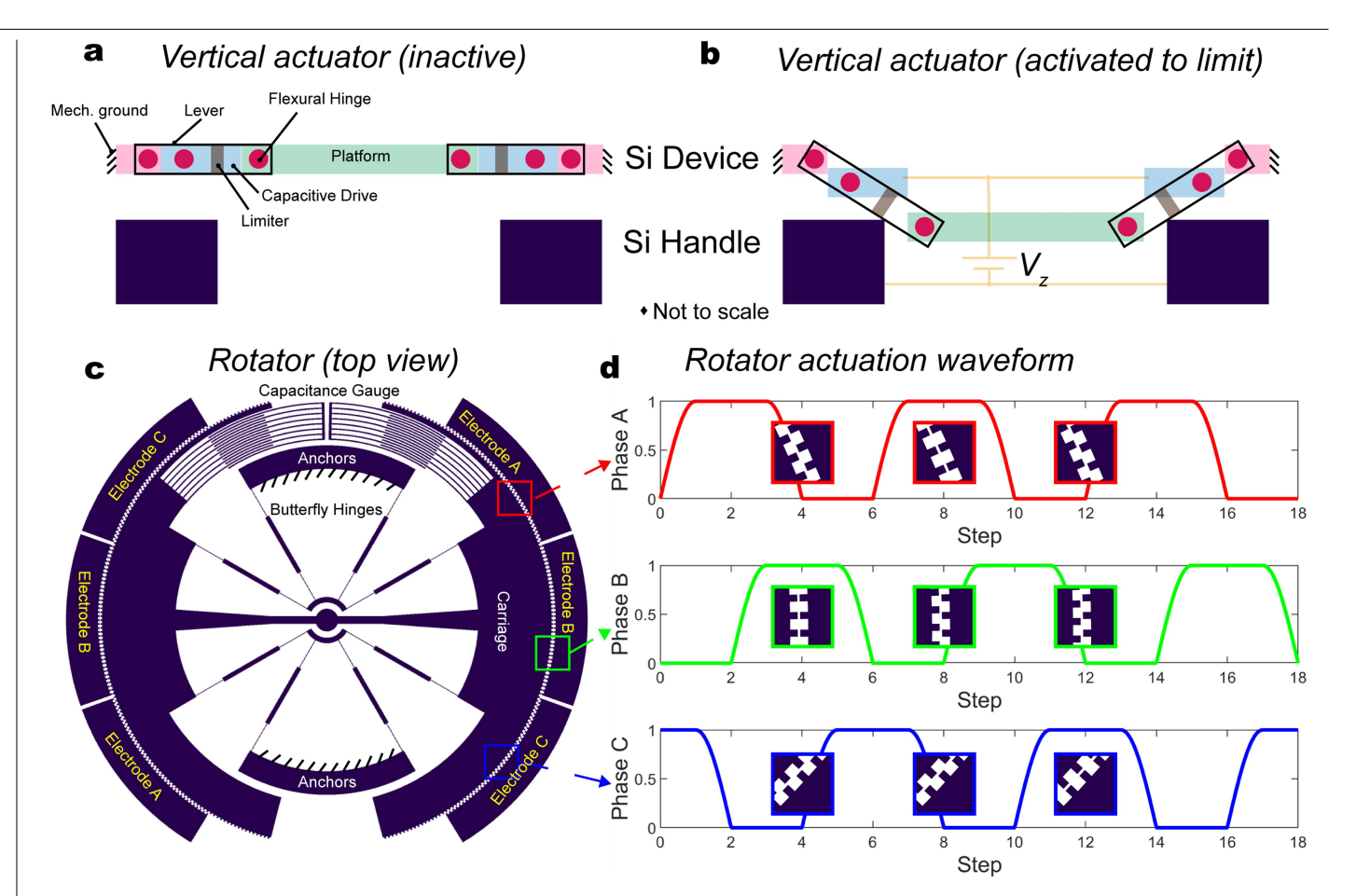
#### Additional information

 $\textbf{Supplementary information} \ The online version contains supplementary material available at https://doi.org/10.1038/s41586-024-07826-x.$ 

Correspondence and requests for materials should be addressed to Eric Mazur, Amir Yacoby or Yuan Cao.

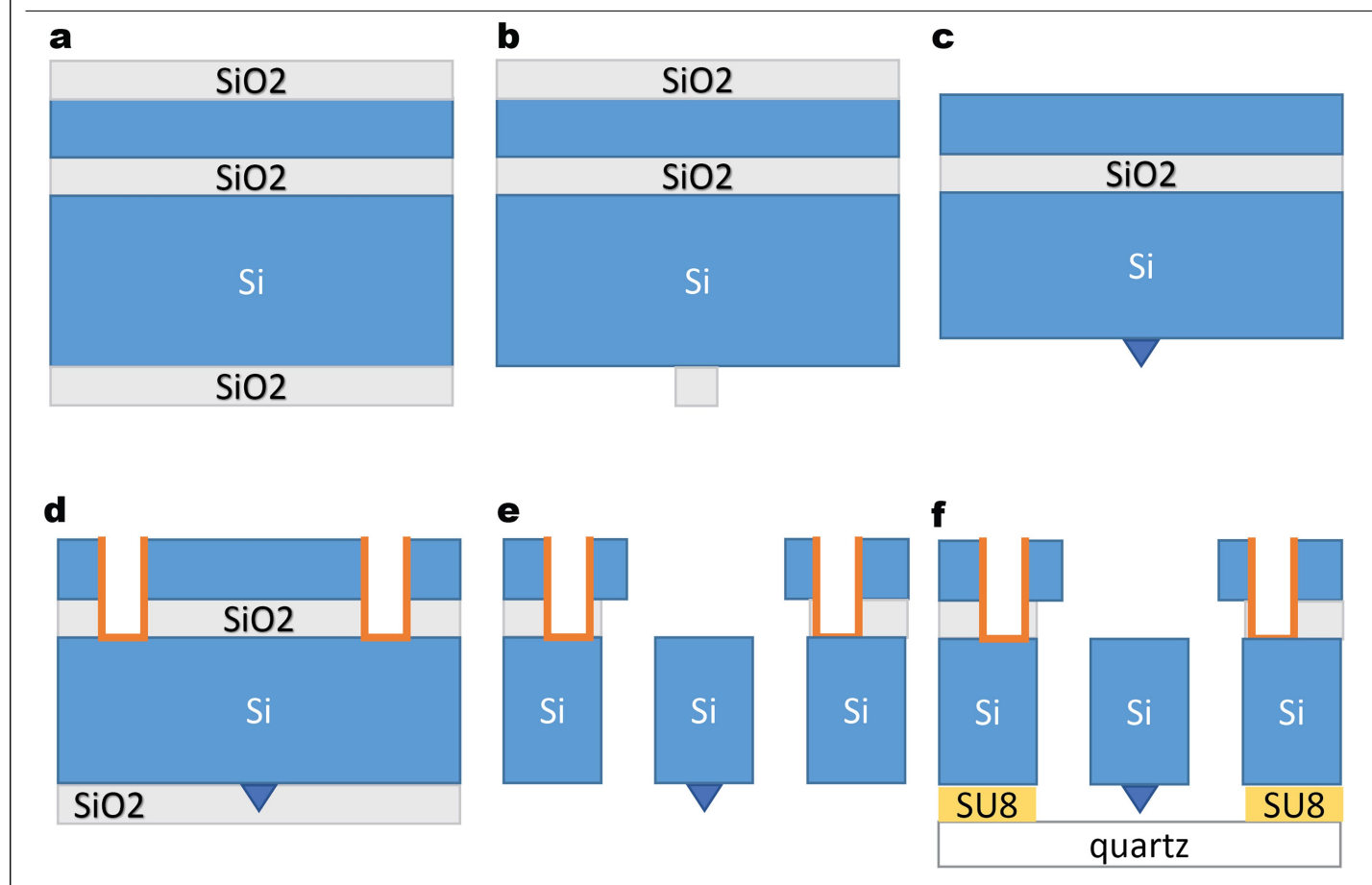
**Peer review information** *Nature* thanks the anonymous reviewers for their contribution to the peer review of this work.

Reprints and permissions information is available at http://www.nature.com/reprints.



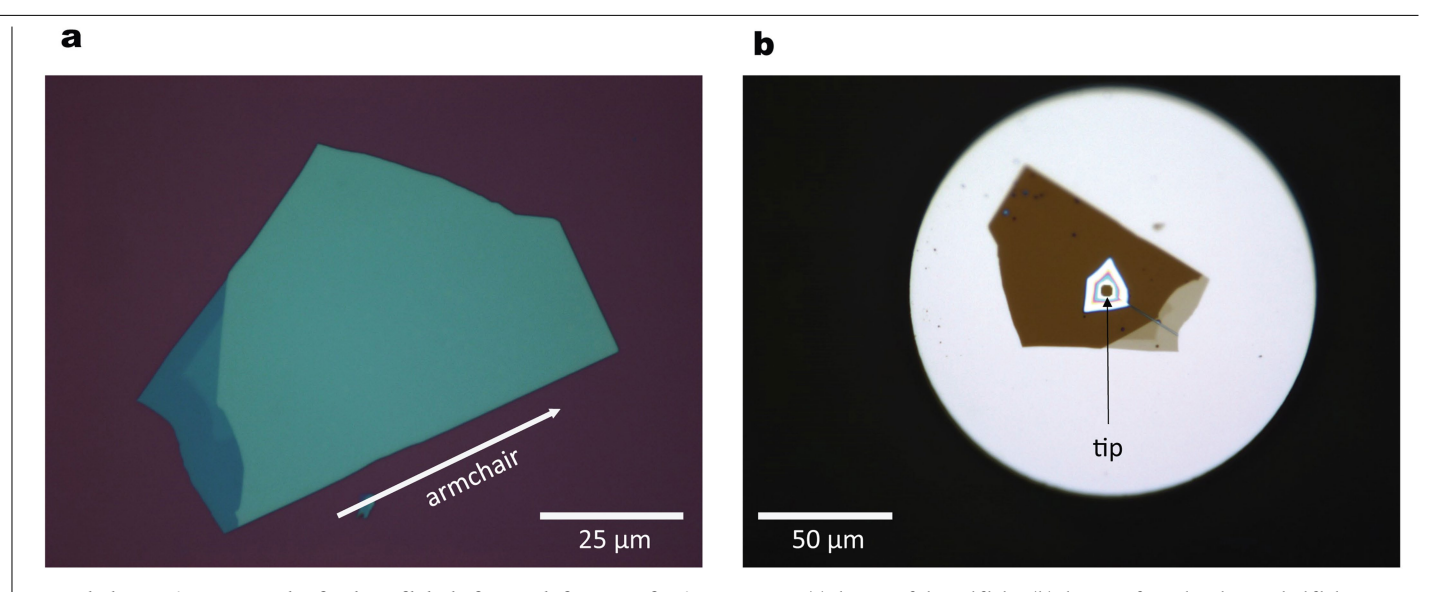
Extended Data Fig. 1 | Illustration of the principle of the vertical actuator and rotary three-phase stepper. (a) Illustration of the vertical actuator at rest position. (b) Vertical actuator driven by a voltage  $V_z$ . (c) Illustration of the rotary

 $\frac{\textbf{actuator with a three-phase electrode.}}{\textbf{for driving the rotary actuator.}} \textbf{The vertical axis is normalised voltage on each phase.}$ 



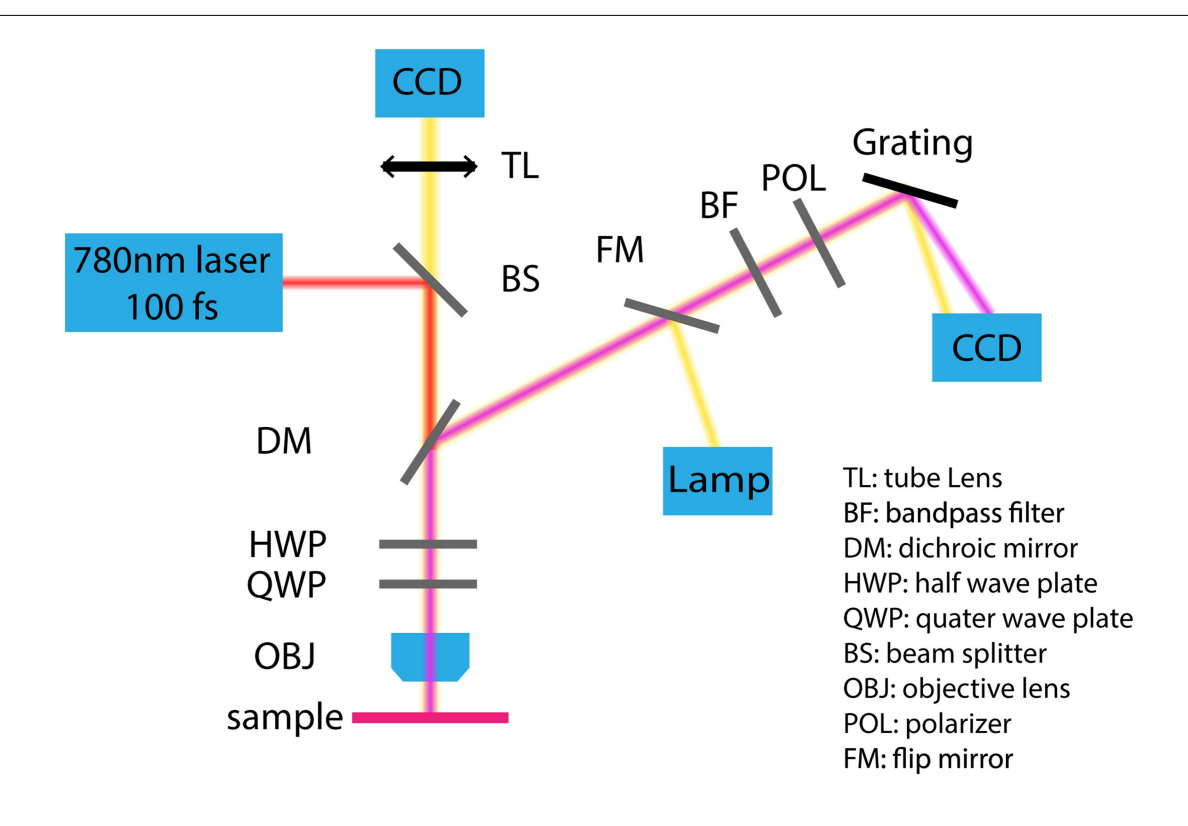
**Extended Data Fig. 2** | **MEMS Fabrication process.** (a) Thermal silicon dioxide is grown on a commercial SOI wafer. (b) Back-side oxide patterning. (c) Tip KOH etching and oxide removal. (d) TSV etching and coating. (e) Back-side and

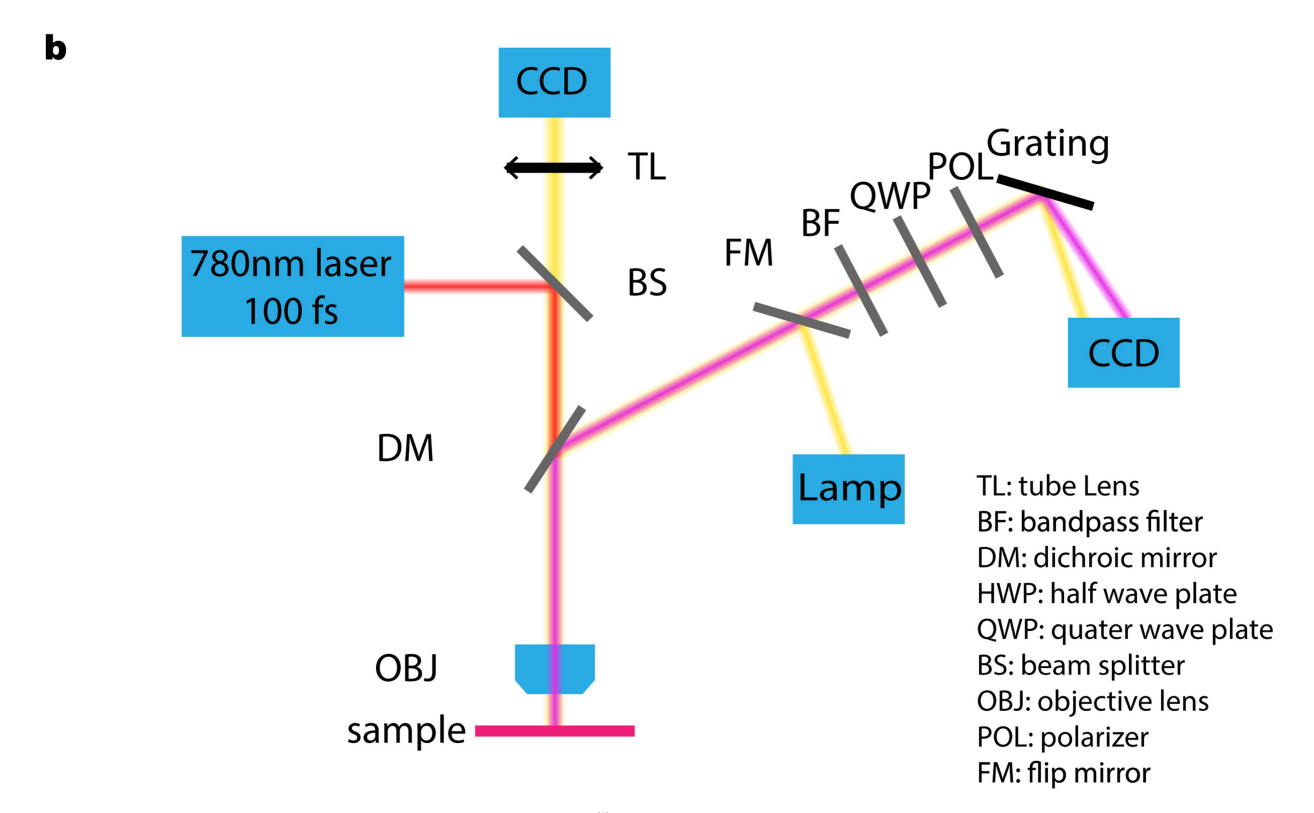
 $front-side\,RIE\,etching\,and\,vapour\,HF\,release.\,(f)\,Bonding\,to\,bottom\,substrate.\\Blue:\,Silicon.\,Gray:\,Silicon\,oxide.\,Orange:\,Poly-silicon.\,Yellow:\,SU-8.$ 



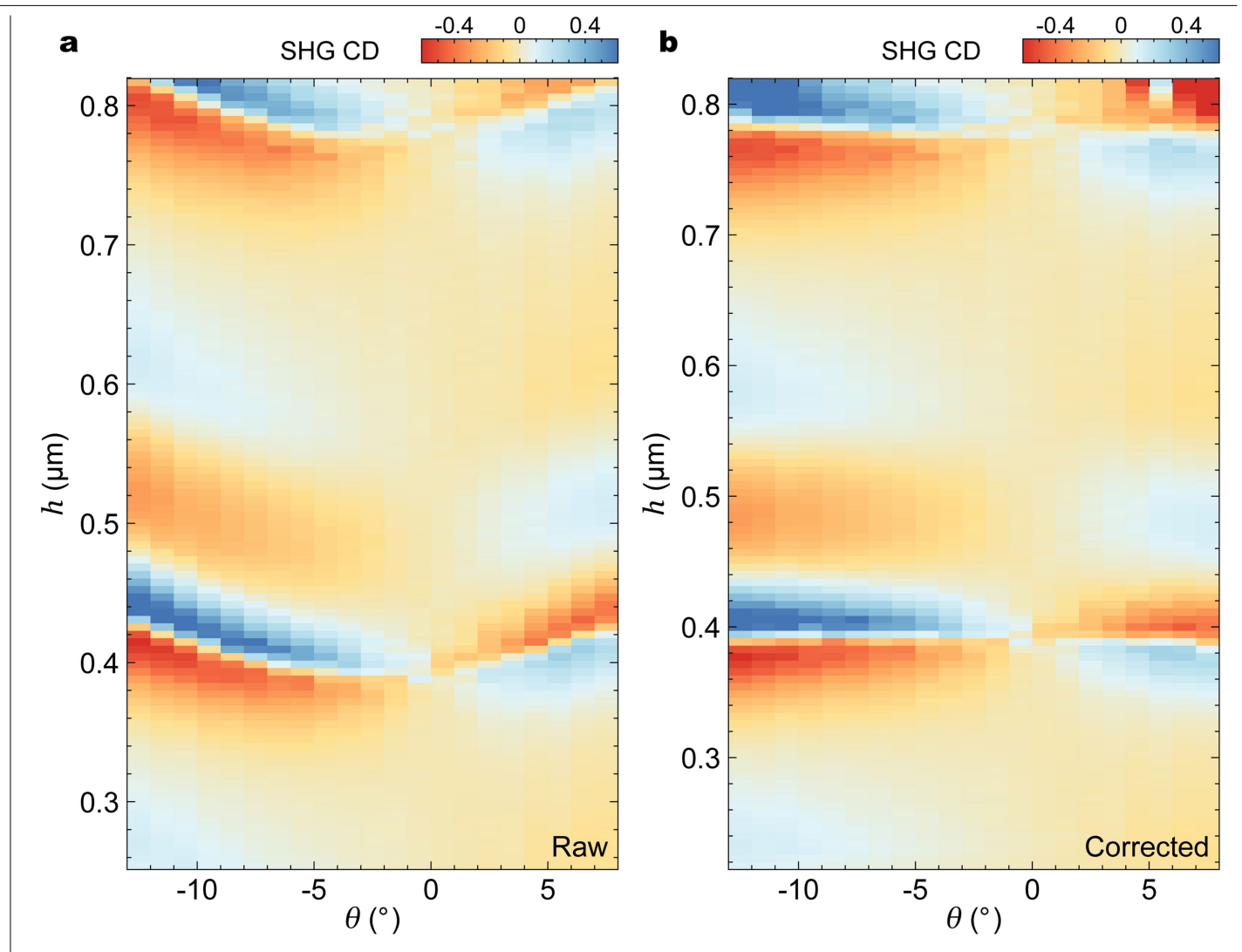
 $\textbf{Extended Data Fig. 3} \\ \textbf{| Example of an h-BN flake before and after transferring to MEMS.} (a) \\ \textbf{the as-exfoliated flake.} (b) \\ \textbf{the transferred and annealed flake.} \\ \textbf{| Example of an h-BN flake before and after transferring to MEMS.} (a) \\ \textbf{| Example of an h-BN flake before and after transferring to MEMS.} (b) \\ \textbf{| Example of an h-BN flake before and after transferring to MEMS.} \\ \textbf{| Example of an h-BN flake before and after transferring to MEMS.} \\ \textbf{| Example of an h-BN flake before and after transferring to MEMS.} \\ \textbf{| Example of an h-BN flake before and after transferring to MEMS.} \\ \textbf{| Example of an h-BN flake before and after transferring to MEMS.} \\ \textbf{| Example of an h-BN flake before and after transferring to MEMS.} \\ \textbf{| Example of an h-BN flake before and after transferring to MEMS.} \\ \textbf{| Example of an h-BN flake before and after transferring to MEMS.} \\ \textbf{| Example of an h-BN flake before and after transferring to MEMS.} \\ \textbf{| Example of a h-BN flake before and after transferring to MEMS.} \\ \textbf{| Example of a h-BN flake before and after transferring to MEMS.} \\ \textbf{| Example of a h-BN flake before and after transferring to MEMS.} \\ \textbf{| Example of a h-BN flake before and after transferring to MEMS.} \\ \textbf{| Example of a h-BN flake before and after transferring to MEMS.} \\ \textbf{| Example of a h-BN flake before and after transferring to MEMS.} \\ \textbf{| Example of a h-BN flake before and after transferring to MEMS.} \\ \textbf{| Example of a h-BN flake before and after transferring to MEMS.} \\ \textbf{| Example of a h-BN flake before and after transferring to MEMS.} \\ \textbf{| Example of a h-BN flake before and after transferring to MEMS.} \\ \textbf{| Example of a h-BN flake before and after transferring to MEMS.} \\ \textbf{| Example of a h-BN flake before a h-BN flake b$ 

a

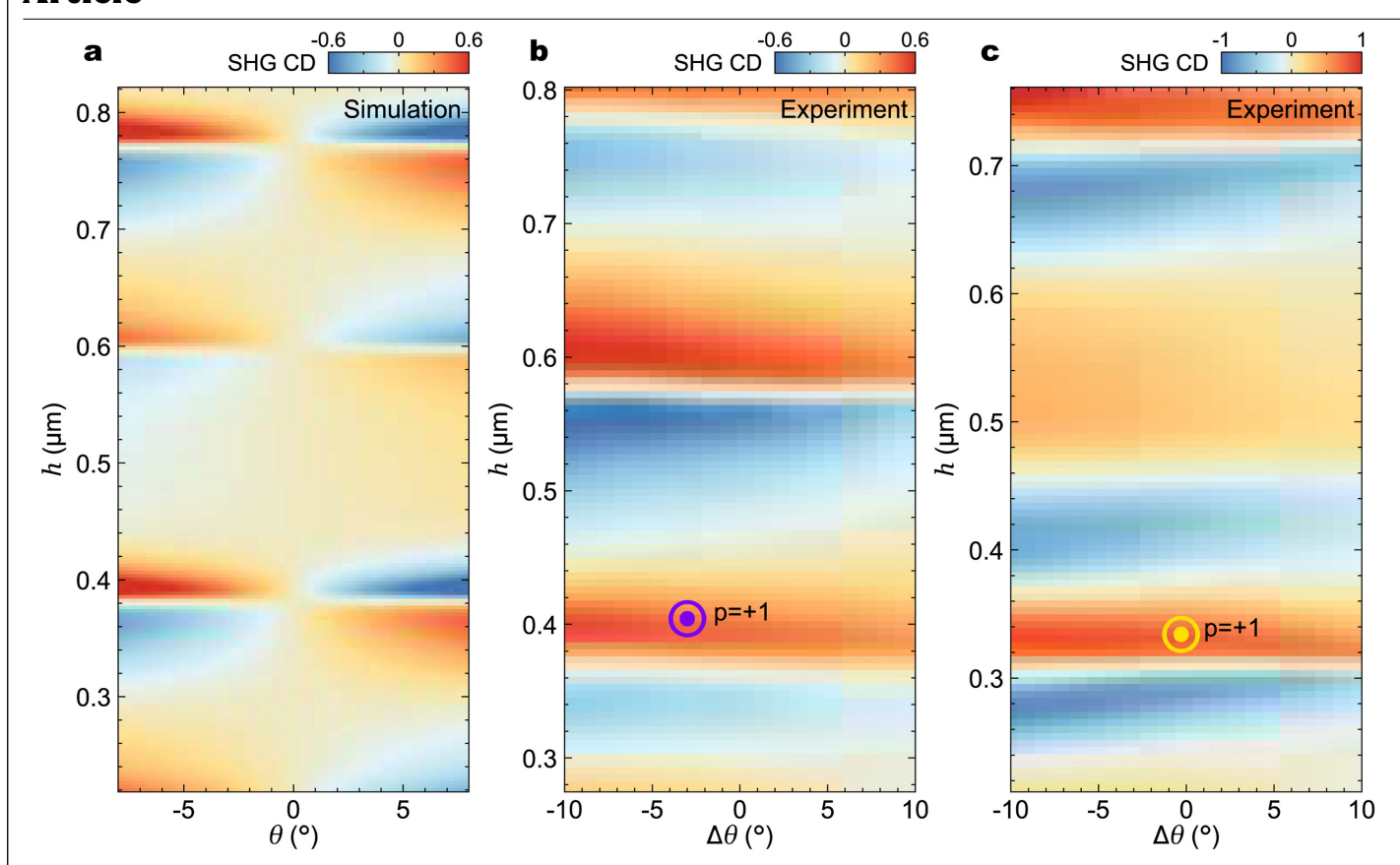




**Extended Data Fig. 4** | **Detailed measurement setups.** (a) Parallel SHG ( $\chi^{(2)}$ ) measurement setup. The quarter wave plate (QWP) before the objective is optional and only used for SHG CD measurements. (b) Quarter-wave plate polarimetry setup for arbitrary polarisation generation.

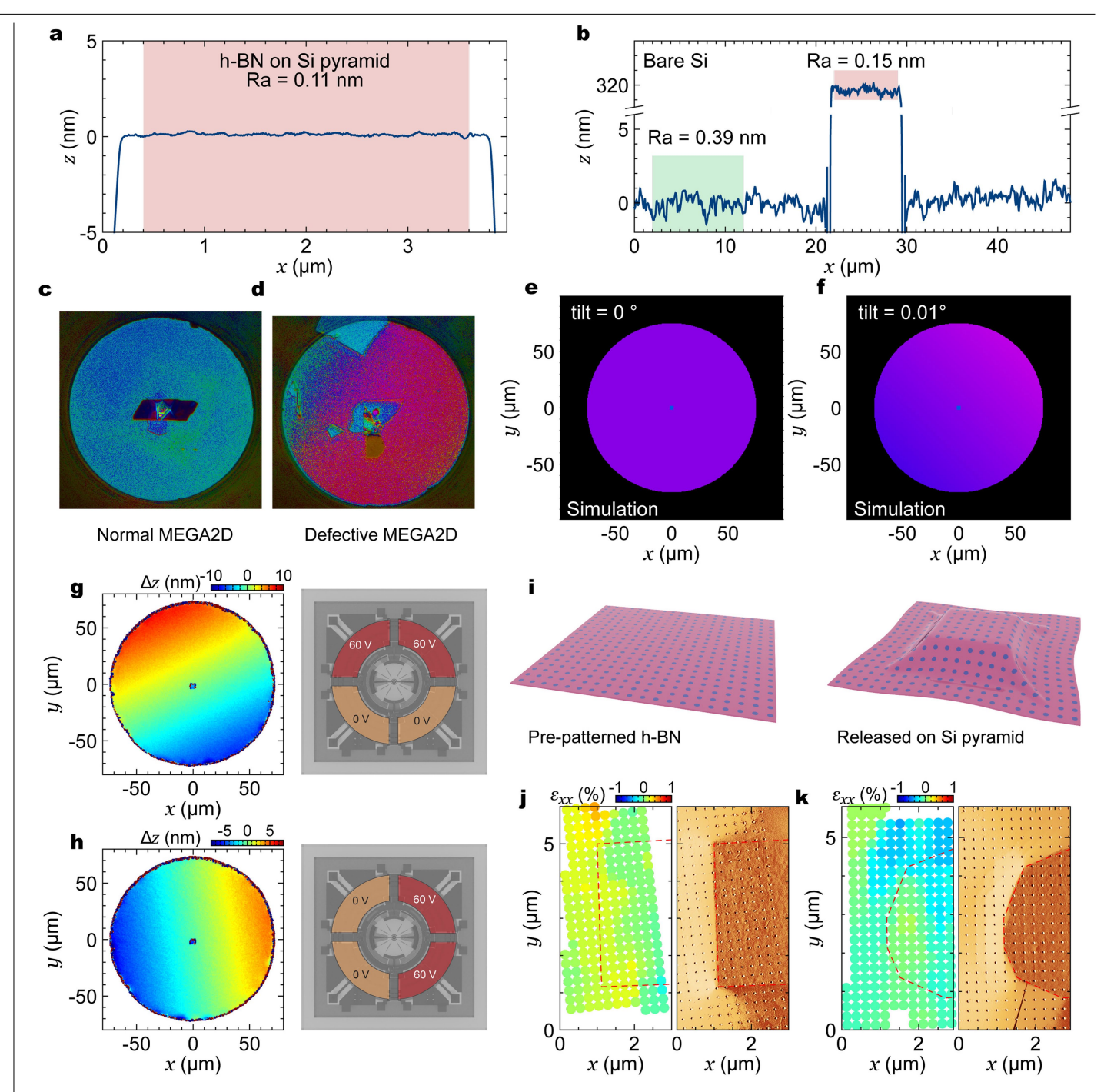


**Extended Data Fig. 5** | **Correction of Z/R crosstalk in measured SHG data.** (a) Raw data of SHG CD corresponding to Fig. 2h. (b) Data corrected for a quadratic drift with respect to  $\theta$ .



 $\label{lem:extended} \textbf{Extended Data Fig. 6} | \textbf{Additional SHG CD simulation and experimental} \\ \textbf{data.} \ (a) \ Simulated \ SHG \ CD \ corresponding to \ Fig. 2h. (b-c) \ Measured \ SHG \ CD \ data \ at the anti-meron (Fig. 3h,i) \ and \ meron (Fig. 3j,k), \ respectively. \ The \ sign \ of \ SHG \ CD \ at the \ meron/anti-meron \ core \ is \ used \ to \ determine \ their \ polarity \ \textit{p},$ 

which is +1 in both cases. Combined with the vorticity (v), which is determined from  $\alpha$  measurements shown in Fig. 3h–k, their meron (Q=+1/2) or anti-meron (Q=-1/2) nature could be pinpointed.



Extended Data Fig. 7 | Interfacial quality of MEGA2D devices. (a) AFM line scan of a clean h-BN flake on a Si pyramid. The average roughness is 0.11 nm over about 4  $\mu m$ . (b) Large-scale AFM line scan of a Si pyramid, showing the parallelism between the Si pyramid (pink) and Si pillar surface (green). While the Si pillar has an increased roughness, the Si pyramid has the intrinsic roughness of a commercial Si wafer. (c-d) The optical image of (c) a normal MEGA2D device and (d) a defective MEGA2D device, taken through the fused silica substrate. The colours are saturated to show the colour variation. Defective devices typically show colour bands that indicate a tilt angle, whereas working devices do not show such bands. (e-f) Simulated colour (saturated) of an air gap

 $(540 \, \mathrm{nm})$  between fused silica and silicon, (e) without tilt and (f) with a tilt of  $0.01^\circ$ . Colour variation can be seen on the upper-right corner of the Si pillar (circle). (g-h) Our MEMS actuators can be driven differentially to tilt the Si pillar/pyramid in either (g) y direction or (h) x direction, by an amount that is on the order of  $0.008^\circ$ . (i) Illustration of patterned h-BN for strain measurements. (j) Extracted strain profile along horizontal direction for a 45 nm thick h-BN flake on square pyramid (denoted by red dashed lines). The right panel shows the raw AFM image (amplitude channel). (k) Same measurements for a rounded pyramid and a 30 nm thick h-BN flake.